Contrasting response of West and East Antarctic ice sheets to Glacial Isostatic Adjustment

Violaine Coulon[1], Kevin Bulthuis[2], Pippa L. Whitehouse[3], Sainan Sun[1], Konstanze Haubner[1], Lars Zipf[1], Frank Pattyn[1]

[1]Laboratoire de Glaciologie, Université Libre de Bruxelles, Brussels, Belgium
[2]Jet Propulsion Laboratory, California Institute of Technology, Pasadena, CA, USA
[3]Department of Geography, Durham University, Durham, UK DH1 3LE

Key Points:

- We developed an elementary GIA model featuring a spatially-varying ELRA model and an approximation to geoid changes
- On multicentennial-to-millennial timescales, GIA feedbacks significantly promote the stability of the WAIS
- On millennial timescales, considering a uniform Antarctic Earth structure may overestimate the stabilizing role of GIA feedbacks in the EAIS

Corresponding author: Violaine Coulon, vcoulon@ulb.ac.be

Abstract

The Antarctic ice sheet (AIS) lies on a solid Earth that displays large spatial variations in rheological properties, with a thin lithosphere and low-viscosity upper mantle (weak Earth structure) beneath West Antarctica and an opposing structure beneath East Antarctica. This contrast is known to have a significant impact on the ice-sheet grounding-line stability. Here, we embed within an ice-sheet model a modified glacial-isostatic Elastic Lithosphere–Relaxing Asthenosphere (ELRA) model that considers a dual pattern for the Earth structure beneath West and East Antarctica supplemented with an approximation of gravitationally-consistent geoid changes, allowing to approximate near-field relative sea-level changes. We show that this elementary GIA model captures the essence of global Self-Gravitating Viscoelastic solid-Earth Models (SGVEMs) and compares well with both SGVEM outputs and geodetic observations, allowing to capture the essential features and processes influencing Antarctic grounding-line stability in a computationally-efficient way. In this framework, we perform a probabilistic assessment of the impact of uncertainties in solid-Earth rheological properties on the response of the AIS to future warming. Results show that on multicentennial-to-millennial timescales, spatial variability in solid-Earth deformation plays a significant role in promoting the stability of the West Antarctic ice sheet (WAIS). However, WAIS collapse cannot be prevented under high-emissions climate scenarios. On longer timescales and for unmitigated climate scenarios, continent-wide mass loss projections may be underestimated because spatially uniform Earth models, as typically considered in numerical ice sheet models, will overestimate the stabilizing effect of GIA across East Antarctica, which is characterized by thick lithosphere and high upper-mantle viscosity.

Plain Language Summary

When an ice sheet loses mass, the pressure it exerts on the underlying solid Earth decreases and the Earth surface rebounds. This process, called glacial isostatic adjustment, is important to consider in ice sheet models because it can stabilize an ice sheet undergoing unstable retreat. Most models consider that the solid Earth response to ice mass changes is uniform. However, because of the weak mantle observed beneath West Antarctica, the isostatic rebound in this region is much faster than previously thought. Oppositely, a slow Earth response is observed in East Antarctica, characterized by a more rigid mantle. In this study, we consider this contrast in the isostatic response of the Antarctic solid Earth and show that it plays a crucial role on the future evolution of the Antarctic ice sheet. More specifically, we find that the rapid Earth response in West Antarctica significantly stabilizes the ice sheet on multicentennial-to-millennial timescales, even though a collapse of the West Antarctic ice sheet cannot be avoided under high-emissions climate scenarios. We also find that the slow Earth response in East Antarctica has an influence on long timescales, potentially leading to an underestimation of future mass loss in the East Antarctic ice sheet.

1 Introduction

The majority of the West Antarctic ice sheet (WAIS) as well as some basins of the East Antarctic ice sheet (EAIS) are grounded below present-day sea level on an inland sloping bed (Fretwell et al., 2013; Morlighem et al., 2019). Such a configuration makes these basins particularly vulnerable to rapid grounding-line retreat that may lead to the so-called ice marine ice sheet instability (MISI) in case of weak or absence of buttressing (Weertman, 1974; Thomas & Bentley, 1978; Mercer, 1978; Schoof, 2007). MISI is triggered when the grounding line is forced to retreat into deeper water, where thicker ice leads to increased ice flux into the ocean, inducing a positive feedback that leads to runaway ice loss. Hence, the Antarctic ice sheet (AIS) has the potential to make a signif-

icant contribution to future sea-level rise (Golledge et al., 2015; Ritz et al., 2015; Bulthuis et al., 2019; Edwards et al., 2019).

However, an inward-deepening marine ice sheet may be stabilized by secondary feedback mechanisms triggered by ice mass changes. Indeed, grounding-line retreat leads to a decrease of the local water depth (expressed as a relative sea-level fall) through glacial isostatic adjustment (GIA), due to the combined effect of (i) a rebound of the unloaded solid Earth and (ii) a drop of the local sea surface (or geoid) induced by a reduction of the gravitational attraction exerted by the shrinking ice sheet on the surrounding ocean (Clark & Lingle, 1977; Mitrovica et al., 2001). As the ice thickness at the grounding line is proportional to the local water depth, the reduction of the local water depth due to GIA has the potential to stabilize a marine ice sheet undergoing MISI (Gomez et al., 2012, 2013, 2015; Konrad et al., 2015; Larour et al., 2019). Moreover, the gradient of the reverse bed slope will be reduced by differential solid-Earth rebound (Adhikari et al., 2014). Feedbacks between GIA and ice dynamics thus have a significant impact on grounding-line stability and must be accounted for when considering the future evolution of the AIS. These feedbacks are ideally taken into account by coupling an ice-sheet model with a self-gravitating viscoelastic solid-Earth model (SGVEM) in which a gravitationally self-consistent sea-level evolution is considered (or coupled ice sheet–sea level–solid Earth deformation models; e.g., de Boer et al., 2014; Konrad et al., 2015; Gomez et al., 2015, 2020). However, this comes at the expense of a significant computational cost.

The strength of GIA feedbacks depends on the pattern and the rate at which the solid Earth responds to ice-sheet changes. Both depend in turn on the rheological properties of the solid Earth, in particular the lithosphere thickness and the upper mantle viscosity, respectively. Several studies have shown that the AIS lies on a region of the solid Earth that is characterized by a strong lateral variability in rheological properties, with a thin lithosphere and a low-viscosity upper mantle beneath West Antarctica and a thick lithosphere and a more viscous upper mantle beneath East Antarctica (Ritzwoller et al., 2001; Morelli & Danesi, 2004; Heeszel et al., 2016; Chen et al., 2018; Pappa et al., 2019; Lloyd et al., 2020). A low-viscosity upper mantle and a thin lithosphere (referred to as a weak Earth structure), as observed under the WAIS, will produce a faster and more localized viscoelastic response of the solid Earth to ice-load changes (contrary to a thicker lithosphere that acts to dampen and smooth the solid-Earth response or a high-viscosity upper mantle that generates a slower response), hence emphasizing the local relative sea-level fall and facilitating stabilizing feedbacks (Gomez et al., 2015; Konrad et al., 2016). More specifically, recent evidence suggests very low mantle viscosities in some areas of West Antarctica, inducing solid-Earth response times on decadal rather than millennial timescales (Nield et al., 2014; Barletta et al., 2018), which is orders of magnitude faster than previously assumed. The West–East dichotomy in Antarctic Earth structure may play a crucial role in the future evolution of the AIS (Kaufmann et al., 2005; van der Wal et al., 2015; Hay et al., 2017; Nield et al., 2018) and should be accounted for. However, major uncertainties remain in determining rheological properties of the Antarctic solid Earth with precision and absolute values of mantle viscosity and lithosphere thickness remain poorly constrained (van der Wal et al., 2015; Hay et al., 2017; Gomez et al., 2018; Whitehouse et al., 2019). An additional complicating factor is that accounting for lateral variations in Earth structure leads to a considerable increase in computational cost, which explains why, apart from some exceptions (e.g., Gomez et al., 2018), most coupled ice sheet–solid Earth models omit them.

Here, we develop a regional elementary GIA model that includes (i) an Elastic Lithosphere–Relaxing Asthenosphere (ELRA) model that mimics the West–East dichotomy in Antarctic Earth structure and (ii) a gravitationally-consistent description of the sea surface (geoid) near the margin of ice sheets that accounts for local mass changes. We take advantage of the computational efficiency of this simplified Earth model to assess in a probabilistic way the impact of uncertainties in the Antarctic viscoelastic properties on the response

of the AIS to climate forcing. More specifically, we use an ensemble of 2000 Monte Carlo simulations that span a range of plausible solid-Earth structures for both WAIS and EAIS. We do not seek to provide new probabilistic projections of the response of the AIS to climate change but rather to quantify how uncertainties in Antarctic solid-Earth rheology translate into uncertainties in the predictions of the future behavior of the AIS.

2 Data and Methods

2.1 Ice-Sheet Model

We perform simulations of the AIS over a time span of 5000 years, starting from present-day geometry, under different warming scenarios with the "fast Elementary Thermomechanical Ice Sheet" model (f.ETISh; Pattyn, 2017) v1.6. All simulations are performed at a spatial resolution of 25 km. In order to account for grounding-line migration, a flux condition (related to the ice thickness at the grounding line; Schoof, 2007) is imposed at the grounding line following the implementation by Pollard and DeConto (2012a). This implementation has been shown to reproduce the migration of the grounding line and its steady-state behavior (Schoof, 2007) at coarse resolution (Pattyn et al., 2013). Numerical simulations of the AIS using a flux condition have also been able to simulate marine ice-sheet behavior in large-scale ice-sheet simulations (Pollard & DeConto, 2012a; DeConto & Pollard, 2016; Pattyn, 2017; Sun et al., 2020). While the use of such a flux condition has been challenged, especially with respect to ice shelf buttressing and regimes of low driving and basal stresses (Haseloff & Sergienko, 2018; Pegler, 2018; Reese et al., 2018; Sergienko & Wingham, 2019), Pollard and DeConto (2020) demonstrate that the algorithm gives similar results under buttressed conditions compared to high-resolution models. The model is initialized for present-day conditions in the way described by Pollard and DeConto (2012b). For the forcing runs, the initial steady-state ice sheet is perturbed by atmospheric and ocean warming for a period of 5000 years. The atmospheric warming is defined based on four extended representative concentration pathway (RCP) temperature scenarios for Antarctica (Golledge et al., 2015; Bulthuis et al., 2019) that are relevant for the period 2000 to 2300 CE. Forcing is kept constant after 2300 CE for the remainder of the model run. Oceanic warming, influencing basal melting underneath floating ice shelves (determined with the PICO model; Reese et al., 2018) is expressed as an instantaneous change in ocean temperature linearly related to atmospheric temperature changes using a proportionality ratio of 0.3 (Maris et al., 2014; Pattyn, 2017; Bulthuis et al., 2019). This linear ocean-atmosphere relationship has been shown to reproduce trends in Antarctic ocean and air temperatures from the Climate Model Intercomparison Project phase 5 consortium (Golledge et al., 2015). Note that such a relationship does not take into account lag effects between the atmosphere and the ocean. However, this should have little influence on the timescales considered here, especially considering that climate is kept constant beyond 2300 CE. The present-day ice-sheet configuration is assumed to be at steady state. We also make the assumption (further discussed in section 4) that the solid Earth is in equilibrium with the initialized ice load. Additional information on the model setup is given in Appendix A.

2.2 Elementary GIA Model

Due to GIA feedbacks, changes in relative sea level – i.e., the difference between the sea surface (or geoid) and the bedrock – at the grounding line will strongly deviate from global mean sea-level change during near-field ice-sheet changes. However, while numerical ice-sheet models commonly consider the deformation of the solid Earth, they rarely account for spatially-variable changes in sea-surface height. Instead, they are typically run assuming that the sea surface adjacent to an ice sheet is uniform, either remaining constant or tracking global mean sea-level changes. The simplified GIA model presented in this paper is a regional model that approximates gravitationally-consistent

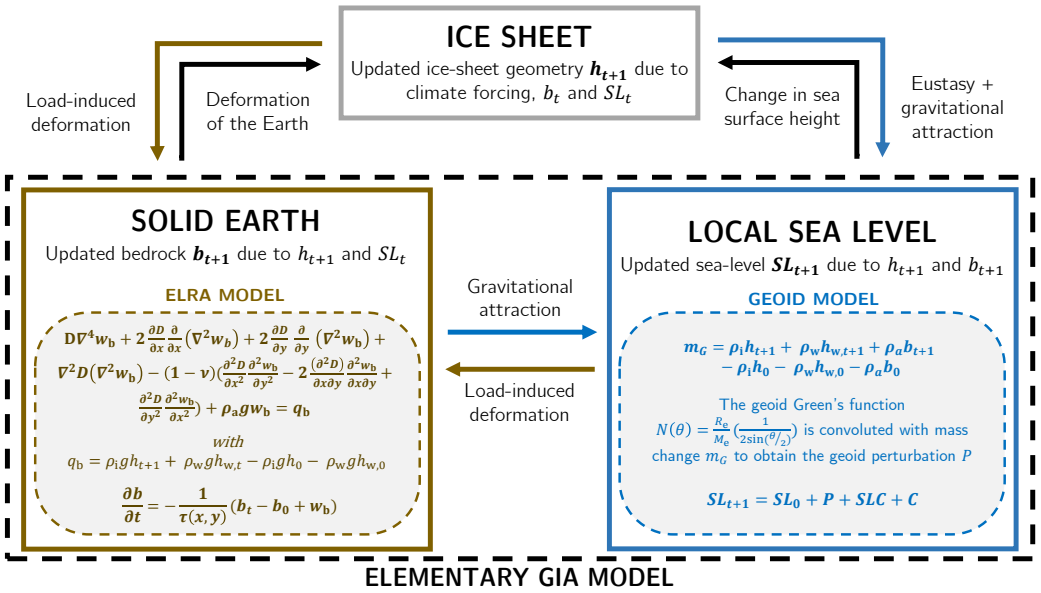

Figure 1. Interactions between the ice sheet, the local sea level, and the solid Earth in the regional coupled system described here, adapted from de Boer et al. (2017). In the solid-Earth system, $D(x, y)$ is the flexural rigidity of the lithosphere, ν the lithospheric Poisson's ratio, w_b the equilibrium deflection of the lithosphere, q_b the applied load, g the gravitational acceleration, and $\tau(x, y)$ the relaxation time of the asthenosphere. In addition, ρ_i, ρ_w, and ρ_a are the ice, ocean water, and asthenosphere densities, respectively. The ocean column thickness at time steps t and $t + 1$ are $h_{\mathrm{w},t} = SL_t - b_t$ and $h_{\mathrm{w},t+1} = SL_t - b_{t+1}$, respectively, while h_t and h_{t+1} are the ice thicknesses at time t and $t + 1$ and h_0 and $h_{\mathrm{w},0}$ are the initial ice and ocean column thicknesses. Similarly, b_0 is the initial bedrock elevation and b_t and b_{t+1} the ones at time t and $t + 1$. In the local sea-level system, R_e and M_e are the Earth radius and mass, respectively, and θ is the spherical distance from the load. SLC is the barystatic sea-level contribution due to ice sheet mass changes, and C is a mass conservation term.

relative sea-level changes beneath or proximal to the modeled ice sheet. They are approximated by coupling both the solid Earth (bedrock) and gravitational sea-surface (geoid) responses with the ice-sheet model as depicted in Figure 1, allowing for a more realistic sea-level forcing to be applied at the grounding line. More specifically, relative sea-level changes are expressed as the sum of bedrock changes (calculated as a delayed viscous response, see section 2.2.1) and an instantaneous local sea-level change (section 2.2.2) driven by regional mass changes. Other (global) effects such as sea-level changes due to changes in Earth rotation and melting of ice masses other than the AIS are not included. The complete sea-level equation (Farrell & Clark, 1976) is not solved here, as the deformation of the whole Earth surface is not considered.

2.2.1 Solid-Earth Deformational Response

The solid-Earth component of our elementary GIA model is an adaptation of the commonly used Elastic Lithosphere–Relaxed Asthenosphere (ELRA) model (equations (1)-(4)) where the solid-Earth system is approximated by a thin elastic lithosphere plate lying upon a relaxing viscous asthenosphere (Brotchie & Silvester, 1969; Le Meur & Huybrechts, 1996). The response of the bedrock to changing ice and ocean loads is solved through a combined time-lagged asthenosphere relaxation toward isostasy and elastic

lithosphere response due to the applied load (Huybrechts & De Wolde, 1999; Pollard & DeConto, 2012a; Konrad et al., 2014). Assuming that the elastic properties and the thickness of the lithosphere are constant throughout the plate, the equilibrium deflection of the lithosphere w_b (taken positive downwards) is given by the following fourth-order differential equation

$$D\nabla^4 w_\mathrm{b} + \rho_\mathrm{a} g w_\mathrm{b} = q_\mathrm{b}, \tag{1}$$

where D is the flexural rigidity of the lithosphere (related to the lithosphere thickness), ∇^4 the bilaplacian operator, g the gravitational acceleration, ρ_a the asthenospheric density, and q_b the applied ice and ocean load distribution. Here, q_b is expressed as

$$q_\mathrm{b} = \rho_\mathrm{i} g h + \rho_\mathrm{w} g h_\mathrm{w} - \rho_\mathrm{i} g h_0 - \rho_\mathrm{w} g h_{\mathrm{w},0}, \tag{2}$$

where h and h_w are the ice and ocean column thicknesses, respectively, ρ_i is the ice density, ρ_w is the ocean water density, and h_0 and $h_{\mathrm{w},0}$ are the initial values of the ice and ocean column thicknesses, respectively, taken as present-day observations. The values of the parameters are reported in Table A1. Note that if changes in ice thickness and water depth induce a transition from grounded to floating ice, only changes in ocean column will influence the load. Equation (1) is traditionally solved using the Green's function formalism (Huybrechts & De Wolde, 1999; Pollard & DeConto, 2012a). The Green's function corresponds to the solution of equation (1) when the applied load q_b is taken as a point load P_b. Its analytical expression as a function of the distance r from the point load is given by (Greve & Blatter, 2009)

$$G(r) = -\frac{P_\mathrm{b} L_w^2}{2\pi D} \mathrm{kei}\left(\frac{r}{L_w}\right), \tag{3}$$

where kei is a Kelvin function of zeroth order (Brotchie & Silvester, 1969) and $L_w = (D/\rho_\mathrm{a} g)^{1/4}$ is the flexural length scale. For any arbitrary load distribution q_b, the equilibrium deflection of the lithosphere w_b is then expressed as the convolution of the load q_b with the Green's function G. The use of this Green's function provides an efficient way to solve for the deflection of the lithosphere due to ice loading in numerical ice-sheet models in the case of a plate with a constant thickness.

Finally, the rate of change of the bedrock elevation is given by a simple relaxation scheme (Brotchie & Silvester, 1969):

$$\frac{\partial b}{\partial t} = -\frac{1}{\tau}(b - b_0 + w_\mathrm{b}), \tag{4}$$

where b is the bedrock elevation, b_0 is the initial bedrock elevation (taken from modern observed fields and assumed to be in equilibrium with present-day ice and ocean loads), and τ is the relaxation time of the asthenosphere.

The ELRA model commonly considers uniform values for the flexural rigidity of the lithosphere D and the relaxation time of the asthenosphere τ (e.g. in Konrad et al., 2014; DeConto & Pollard, 2016; Pattyn, 2017; Pollard et al., 2017). From a physical point of view, the flexural rigidity and the relaxation time depend on the thickness of the lithosphere and the viscosity of the upper mantle, respectively. Indeed, the flexural rigidity can be related to the effective elastic thickness of the lithosphere h_e, i.e., the portion of the lithosphere that behaves elastically, by (Brotchie & Silvester, 1969)

$$D = \frac{E h_e^3}{12(1-\nu^2)}, \tag{5}$$

where E and ν are constant elastic parameters, namely the Young's modulus and Poisson's ratio, respectively. Separately, it has been shown that, under some assumptions (see section 2.2.3), the solid-Earth relaxation time is approximately proportional to the viscosity of the mantle (Lingle & Clark, 1985; Turcotte & Schubert, 2002; Lowrie, 2007). By fitting an ELRA model to an SGVEM with a 100-km thick Antarctic lithosphere and an upper-mantle viscosity of 5×10^{20} Pa s (i.e., close to what is commonly assumed for a 1-D viscoelastic solid Earth; Gomez et al., 2013; Argus et al., 2014; Pollard et al., 2017; de Boer et al., 2017), Le Meur and Huybrechts (1996) determined corresponding uniform values of 10^{25} N m for D and 3000 years for τ. Since then, these reference values (e.g., Pollard & DeConto, 2012b; de Boer et al., 2015; DeConto & Pollard, 2016; Pattyn, 2017; Pollard et al., 2017; Quiquet et al., 2018) or values close to them (Bueler et al., 2007; Maris et al., 2014) have been widely used in the literature.

Here, we account for the characteristic configuration of the Antarctic solid Earth by using spatially-varying flexural rigidity $D(x, y)$ and relaxation time $\tau(x, y)$. For this purpose, the standard ELRA model described above is adapted in order to consider a plate with spatially-varying thickness $h_e(x, y)$ i.e.,

$$D(x, y) = \frac{E h_e^3(x, y)}{12(1-\nu^2)}. \tag{6}$$

The deflection of a plate having a spatially-varying flexural rigidity and lying on a viscous mantle then becomes

$$\begin{aligned} &D\nabla^4 w_\mathrm{b} + 2\frac{\partial D}{\partial x}\frac{\partial}{\partial x}(\nabla^2 w_\mathrm{b}) + 2\frac{\partial D}{\partial y}\frac{\partial}{\partial y}(\nabla^2 w_\mathrm{b}) + \nabla^2 D(\nabla^2 w_\mathrm{b}) \\ &-(1-\nu)\left(\frac{\partial^2 D}{\partial x^2}\frac{\partial^2 w_\mathrm{b}}{\partial y^2} - 2\frac{\partial^2 D}{\partial x \partial y}\frac{\partial^2 w_\mathrm{b}}{\partial x \partial y} + \frac{\partial^2 D}{\partial y^2}\frac{\partial^2 w_\mathrm{b}}{\partial x^2}\right) + \rho_\mathrm{a} g w_\mathrm{b} = q_\mathrm{b}. \end{aligned} \tag{7}$$

Equation (7), which is a generalization of equation (1) to a spatially-varying flexural rigidity $D(x, y)$, can be derived formally from thin plate theory (more details are given in Supporting Information Text S1) assuming lateral variations of $D(x, y)$ to be sufficiently smooth (Van Wees & Cloetingh, 1994; Ventsel & Krauthammer, 2001) and has been already used (with success) to represent the deformation of the solid Earth in Garcia et al. (2014). Nonetheless, it has not been used so far to simulate the deformation of the solid Earth in ice-sheet models. Equation (7) can no longer be solved using the Green's function formalism and requires numerical methods such as finite differences or finite elements. Contrary to the Elastic Lithosphere model, the Relaxing Asthenosphere part of the ELRA model is a local model. Equation (4) thus remains valid when considering a spatially-varying and continuous relaxation time $\tau(x, y)$. Note, however, that displacement at any location is influenced by nearby relaxation times. In order to avoid nonphysical discontinuity in the displacement, lateral variations of $\tau(x, y)$ must be sufficiently smooth.

In this context, we attribute distinct uniform values of τ and D to West and East Antarctica, with a smoothing (Gaussian filter) applied at the boundary between the two regions (see Figure 2). Our goal is not to consider realistic average values of $\tau(x, y)$ and $D(x, y)$ over these respective regions, but rather to investigate the sensitivity to a broad range of values that can potentially be observed locally within these different characteristic regions. In accordance with geophysical observations (e.g., Ritzwoller et al., 2001; Morelli & Danesi, 2004; Heeszel et al., 2016; Chen et al., 2018; Lloyd et al., 2020; Pappa

et al., 2019), we attribute lower values of both τ and D beneath WAIS and higher values beneath EAIS (Table 1). The very low mantle viscosities ($10^{18}-10^{19}$ Pa s) estimated in some areas of West Antarctica (i.e., Amundsen Sea Coast, Antarctic Peninsula, and Marie Byrd Land; Barletta et al., 2018; Nield et al., 2014; Lloyd et al., 2020) correspond to very short relaxation times, on the order of years to hundreds of years (Nield et al., 2014; Konrad et al., 2016; Barletta et al., 2018; Whitehouse et al., 2019), while the mantle viscosities of 10^{22} to 10^{23} Pa s observed beneath the lithosphere of inner East Antarctica (Kaufmann et al., 2005; Whitehouse et al., 2019) could be associated to relaxation times on the order of tens of thousands of years. At the boundary between both regions, reconstructed maps of viscosity in Antarctica suggest an upper-mantle viscosity close to $5\times10^{20}-1\times10^{21}$ Pa s (Kaufmann et al., 2005; van der Wal et al., 2015; Pappa et al., 2019; Whitehouse et al., 2019), corresponding to millennial relaxation timescales (Le Meur & Huybrechts, 1996; Argus et al., 2014; Konrad et al., 2016). These values also correspond to the upper-mantle viscosity values that are typically considered in spatially-homogeneous GIA models in order to represent the whole Antarctic continent (Argus et al., 2014; Pollard et al., 2017; de Boer et al., 2017; Garbe et al., 2020). Note that we make the important assumption that the single asthenosphere relaxation time at a location is proportional to the local mean upper mantle viscosity. For the flexural rigidity, various studies in North America and Eurasia have inferred values ranging from $D = 10^{22}$ N m for oceanic lithosphere to $D = 10^{25}$ N m for cratonic lithosphere (e.g., Walcott, 1970; Fjeldskaar, 1997; Audet & Mareschal, 2004; Perez-Gussinye & Watts, 2005). For East Antarctica, Stern and ten Brink (1989) estimated a maximum flexural rigidity of about $D = 10^{25}$ N m (one of the highest values for continental rigidity). On the other hand, they estimated the flexural rigidity for the Ross Embayment in West Antarctica to be more than 2 orders of magnitude less, at $D = 4 \times 10^{22}$ N m. It is important to underline that elastic lithosphere thickness varies as a function of the timescale of the surface loading considered (Nield et al., 2018). Estimates from studies considering processes occurring at different timescales cannot thus straightforwardly be compared. Nevertheless, they give us estimates of both the magnitude of lateral variations and the remaining uncertainty. In this study, we determine ranges of values of D for West and East Antarctica based on values of the elastic lithosphere thickness (equation (6)), with low values of only a few kilometers to a few tens of kilometers estimated in West Antarctica, and predominantly high values in East Antarctica, up to about 150 km (Chen et al., 2018; Pappa et al., 2019). Note that the uniform reference value of $D = 10^{25}$ N m defined by Le Meur and Huybrechts (1996) and widely used since then (e.g., Pollard & DeConto, 2012a; de Boer et al., 2015; Pollard et al., 2017; Pattyn, 2017; Quiquet et al., 2018; Bulthuis et al., 2019) lies close to the maximum flexural rigidity estimated for East Antarctica.

With regards to these geophysical evidences and to properly account for both the large variations observed in mantle viscosity and lithosphere thickness and the associated uncertainty, we consider a wide range of values that span several orders of magnitude (see Table 1).

2.2.2 Geoid Response

A major drawback of the ELRA approximation is that it does not account for local perturbations in the height of the sea surface, thus missing an important feedback process (Konrad et al., 2016). We therefore implemented an approximation of gravitationally-consistent non-uniform sea-level variations due to regional mass changes m_G, here expressed as

$$m_G = \rho_\mathrm{i} h + \rho_\mathrm{w} h_\mathrm{w} + \rho_\mathrm{a} b - \rho_\mathrm{i} h_0 - \rho_\mathrm{w} h_{\mathrm{w},0} - \rho_\mathrm{a} b_0. \tag{8}$$

The distribution of mass changes (m_G) is influenced by changes in the ice and/or ocean column (depending on whether a specific location is covered by grounded ice or by ocean water) as well as by changes in bedrock elevation. Mass changes associated with

Table 1. Solid-Earth parameters in the ELRA model with their uncertainty ranges used in the uncertainty analysis. Uncertainty ranges of associated viscoelastic properties are provided for the sake of illustration, but should not be considered as exactly equivalent. We consider wide ranges of values in order to account for the large variations observed locally and the associated uncertainty.

Solid-Earth parameter	Uncertainty range	Units	Associated viscoelastic property	Uncertainty range	Units
WAIS relaxation time (τ_{W})	$1 \times 10^{0} - 5 \times 10^{3}$	yr	WAIS mantle viscosity	$\sim 10^{18} - 10^{21}$	Pa s
EAIS relaxation time (τ_{E})	$1 \times 10^{3} - 5 \times 10^{4}$	yr	EAIS mantle viscosity	$\sim 10^{20} - 5 \times 10^{22}$	Pa s
WAIS flexural rigidity (D_{W})	$1 \times 10^{22} - 1 \times 10^{24}$	N m	WAIS effective elastic lithosphere thickness	$\sim 10 - 50$	km
EAIS flexural rigidity (D_{E})	$5 \times 10^{23} - 5 \times 10^{25}$	N m	EAIS effective elastic lithosphere thickness	$\sim 40 - 150$	km

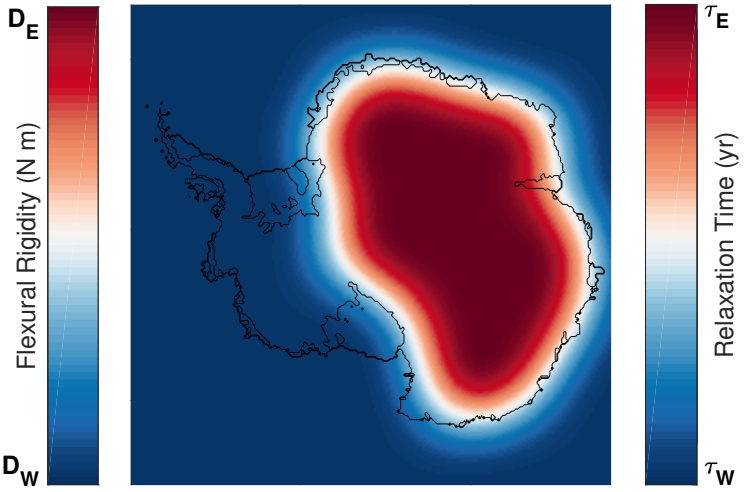

Figure 2. Dual pattern for the ELRA solid-Earth parameters – Flexural rigidity D (N m) and Relaxation time τ (yr) – approximating lateral variations between East and West Antarctica. The values of D_{W} and τ_{W} are applied to the dark blue areas while the values of D_{E} and τ_{E} are applied to the red areas. Smoothing (Gaussian filter) is applied at the boundary between the two regions. The values of D_{W}, τ_{W}, D_{E} and τ_{E} are sampled from Table 1. Note that following geophysical evidence (e.g., Nield et al., 2018; Lloyd et al., 2020; Pappa et al., 2019) we apply the values of Western Antarctica to the ocean areas outside of the Antarctic continent.

bed elevation change are calculated assuming asthenosphere density, noting that the perturbation in gravitational attraction due to ice and ocean mass changes will be somewhat counterbalanced by the gravitational effect of the subsequent solid-Earth deformation, which arises due to the displacement of mantle material below the lithosphere (Root et al., 2015).

For a unit point mass, the perturbation in the geoid is approximated by

$$N(\theta) = \frac{R_\mathrm{e}}{M_\mathrm{e}} \left(\frac{1}{2\sin(\theta/2)} \right), \tag{9}$$

where $N(\theta)$ is a geoid Green's function, R_e the Earth radius, M_e the Earth mass, and θ the spherical distance from the load point (see Table A1 for their values). Note that equation (9) considers a spherical Earth. This expression is convoluted with the distribution of mass changes m_G in order to obtain the change in geoid height P compared to the initial sea-surface height SL_0 (taken here as present-day sea level). In order to capture the entire geoid perturbation, this convolution is realized over an extended ocean domain. Local sea surface changes are then calculated as the sum of the geoid perturbation P, the barystatic sea-level contribution arising from Antarctic ice mass changes (SLC, calculated as in Goelzer et al., 2020) and a mass conservation term C, which is a spatial constant that must be added to the solution in order to conserve oceanic mass (see Supporting Information Fig. S1). Note that since we calculate geoid changes between discrete configurations of the ice–earth–ocean systems, we approximate the perturbation of the geoid using Green's functions of geoid for a rigid Earth (Farrell & Clark, 1976). In studies that solve the full sea-level equation, self-consistent solutions for geoid and solid Earth perturbations are determined iteratively using Green's functions for a deforming Earth. This approach would significantly increase the computation time of our model and would only lead to a small increase in accuracy. The geoid model defined here only considers gravitational changes directly or indirectly due to changes in Antarctic ice-sheet cover (Figure 1). Sea-level contributions stemming from ice masses other than the AIS are not considered. The feedback due to Earth rotational effects (Milne & Mitrovica, 1998) is also neglected.

2.2.3 Comparison with full Self-Gravitating Earth Models

Within a SGVEM, the response of the solid Earth to changing loads is typically described using a linear Maxwell viscoelastic rheology, with an instantaneous elastic response superposed on a longer-term Newtonian viscous relaxation. The majority of GIA models (including most coupled ice sheet–sea level–solid Earth deformation models) adopt this rheology and consider a spherical Earth, with an elastic lithosphere, a viscoelastically stratified mantle, and an inviscid core (e.g., Gomez et al., 2013, 2015; Adhikari et al., 2014; de Boer et al., 2014; Konrad et al., 2015; Pollard et al., 2017). The elementary GIA model developed in this paper is based on several simplifying assumptions and therefore differs from full GIA models.

A first fundamental simplification is the domain to which it applies: we only consider the AIS and its near-field area while full SGVEMs consider the deformation of the whole Earth, which allows them to solve the sea-level equation for global meltwater distribution. Here, only near-field relative sea-level changes in response to local ice and ocean load changes are considered, while direct and indirect gravitational and earth-deformational effects due to ice masses other than the AIS are neglected. Our simplified model thereby does not comply with mass conservation in the whole Earth system as compared to models able to solve the sea-level equation (Adhikari et al., 2020). In addition, it follows that the sphericity of the Earth is neglected: the solid Earth deformational response considered here (ELRA) is by definition a *flat earth* model, as opposed to spherical earth models. It has been demonstrated that flat-earth models work well within the margin of loads

as large as the Fennoscandian ice sheet (Wolf, 1984) but for larger loads the flat-earth approximation progressively breaks down as the effects of sphericity become increasingly important (Wu & Johnston, 1998).

Because of their viscoelastic layering, SGVEMs capture the full multi-normal-mode response of the Earth to surface loading (Gomez et al., 2013; Whitehouse et al., 2019). Indeed, the larger the load, the deeper its deformation reaches into the mantle. The ease with which the mantle relaxes (i.e., its relaxation time) is thus dependent on the radial viscosity profile, the shallower layers being the more relevant at the local spatial scale (Barletta et al., 2018). In contrast, our simplified GIA model considers an elastic plate lithosphere lying upon a unilayered viscous mantle. The depth-variability of the Earth structure within the mantle (implying a full spectrum of relaxation times) is thus ignored. In the case of a unilayered mantle, the Earth response time can be obtained analytically from the single viscosity value (Barletta et al., 2018), as the relaxation time of the Earth is approximately proportional to the viscosity (Lingle & Clark, 1985). It follows that the $\tau(x, y)$ values used in our model each describe a single relaxation time which does not vary temporally and that is considered proportional to the mean upper-mantle viscosity. In reality, the relaxation time is a function of the wavelength of the ice load, even if the mantle has a homogeneous viscosity (Wu & Peltier, 1982).

Another important assumption lies in the fact that the elastic lithosphere considered in the ELRA model deflects but does not compress. As discussed in Bueler et al. (2007), all vertical displacement w_b in this model is thus associated with upper-mantle motion, while the elastic lithosphere spreads the influence of the load. It follows that, while the Earth's response in SGVEMs is typically split into a viscous long-term and an elastic instantaneous contribution, all deformation in our simplified model is governed by viscous timescales. This is appropriate when modeling multi-centennial to millennial-scale deformation, as is done here, but it would not be appropriate if seeking to model ice sheet change at short timescales, where the elastic component can play an important role in controlling ice sheet behavior (Larour et al., 2019). As an exception to this, our model may be suitable for modeling short timescale ice sheet change in regions of low mantle viscosity, where observations of rapid uplift, triggered by contemporary ice loss, suggest that viscous effects play a significant role at short timescales (Nield et al., 2014; Hay et al., 2017; Whitehouse et al., 2019; Powell et al., 2020). In summary, our approach neglects deformation associated with elastic compression of the lithosphere, but this will have a minimal effect on results for low viscosity regions, or over long timescales.

In addition, the ELRA model assumes that there is no elasticity in the mantle. As a consequence, there will be no vertical stresses from the mantle pushing against the lithosphere plate. This effect can play a role in the formation of forebulges, where the lithosphere is partly uplifted by the mantle in the region surrounding the load. Indeed, Konrad et al. (2014) have shown that peripheral forebulges are underestimated for the ELRA model as compared to SGVEMs. Note that lateral flow in the mantle is also not modeled here.

Lastly, as mentioned above, our simplified GIA model neglects the feedback due to Earth rotational effects, which tends to introduce a slight negative feedback in grounding-line migration (Larour et al., 2019).

2.2.4 Feedbacks between GIA Processes and Ice Dynamics

Glacial isostatic adjustment processes approximated by the Elementary GIA model described above influence Antarctic ice mass changes simulated by the ice-sheet model through different feedback mechanisms. First, GIA affects water depth, and hence the position of the transition between grounded and floating ice – the grounding line – as well as the thickness of ice at that transition (Whitehouse et al., 2019). The thickness of ice at the grounding line, in turn, controls the amount of ice flowing across the ground-

ing line (and thereby ice mass changes and grounding-line movements). The ice flux across the grounding line is highly sensitive to the thickness of ice there (Schoof, 2007); a small increase in water depth on a reverse bed slope would result in the migration of the grounding line upstream to a location where ice thickness is greater, leading to a large increase in ice discharge. In addition, relative sea-level changes due to GIA can influence the degree to which ice shelves are able to stabilise the ice sheet. For example, a local decrease in water depth may enhance grounding of the ice shelf at ice rises, thereby stabilising the ice sheet, while an increase in water depth can lead to ungrounding of an ice rise, thus enhancing the ice flow across the grounding line (Matsuoka et al., 2015). GIA can also affect ice dynamics by altering the shape and slope of the bed near the margins of the ice sheet, where ice mass loss is occurring. Finally, GIA processes can influence ice dynamics through the feedback between isostatically-driven ice surface elevation change and surface mass balance. The evolving shapes of the solid Earth and the adjacent geoid thus act as fundamental boundary conditions on the dynamics of the modeled ice sheet.

2.2.5 Model Validation

To assess the validity of our approach, outputs from our elementary GIA model are compared to SGVEM outputs and geodetic observations. In addition, the behavior of our elementary GIA model coupled to the ice sheet model is compared to outputs from coupled ice sheet–solid Earth models.

We first assess how the solid-Earth component of our model (the ELRA model) behaves compared to SGVEMs. More specifically, we compare ELRA-predicted uplift rates associated with the W12 (Whitehouse, Bentley, & Le Brocq, 2012; Whitehouse, Bentley, Milne, et al., 2012) and ICE-6G (Argus et al., 2014) ice-loading histories with the ones reproduced in Figure 10a of Whitehouse, Bentley, Milne, et al. (2012) and Figure 6a in Argus et al. (2014), respectively, where SGVEMs with a uniformly stratified solid Earth (meaning only radially-varying rheology) are used. In order to use ELRA models that reflect the respective solid-Earth configurations used by these SGVEMs, we consider uniform values of τ and D, with a value of $\tau = 8000\,\mathrm{yr}$ for W12 and a value of $\tau = 4000\,\mathrm{yr}$ for ICE-6G (Argus et al., 2014) and a value of $D = 10^{25}\ \mathrm{N\,m}$ for both cases (Le Meur & Huybrechts, 1996). Ice thicknesses for both models were interpolated onto a 25-km resolution Antarctic grid. Since our ELRA model only covers Antarctica, far-field ice-sheet changes are ignored. Ocean load changes over the 122 kyr duration of the model run are implemented using time-varying uniform sea-level reconstructions from Lambeck et al. (2014) and Bintanja and van de Wal (2008). Gravitationally-consistent local sea-level variations are ignored. Despite these simplifications, we show that the ELRA model is capable of reproducing both the pattern and the magnitude of the present-day uplift rates determined with the original Earth models (Whitehouse, Bentley, Milne, et al., 2012; Argus et al., 2014) by using corresponding uniform ELRA parameters, which gives us confidence in the methodology used. The reproduced uplift rate maps and the difference with the corresponding SGVEM outputs are shown in Figure 3.

In a second step, we compare the present-day uplift rates calculated using each of the 2000 spatially-varying solid-Earth configurations of our ensemble (see section 2.3), driven by both W12 and ICE-6G, with observations from Whitehouse, Bentley, Milne, et al. (2012). The maps of uplift rates averaged over the 2000 solid-Earth structures of our ensemble are displayed in Figure 4.

To assess the degree of fit between the reproduced uplift rates and the elastic-corrected GPS observations of GIA-driven uplift, we calculate the weighted root-mean-square (WRMS) error, defined as

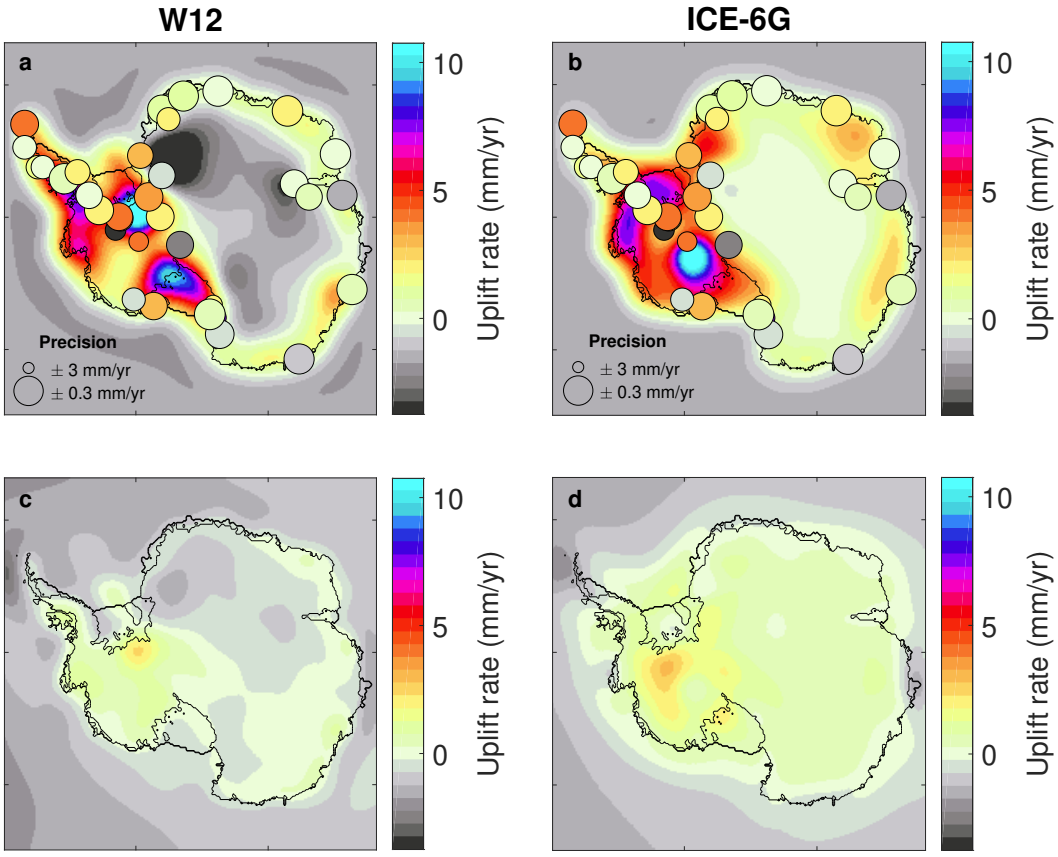

Figure 3. Uplift rate maps for the W12 (a) and ICE-6G (b) ice-loading histories obtained by coupling with an ELRA model using uniform ELRA parameters ($\tau = 8000$ yr and $D = 10^{25}$ N m in (a) and $\tau = 4000$ yr and $D = 10^{25}$ N m in (b), based on Argus et al. (2014) and Le Meur and Huybrechts (1996)). Only the Antarctic component of these ice-loading histories was used while the far-field component, when existent, was ignored. Variations of the ocean load are implemented by a time-varying uniform sea-level based on sea-level reconstructions from Lambeck et al. (2014) and Bintanja and van de Wal (2008). No gravitationally-consistent local sea-level variations are considered. GPS observations of present-day uplift rates (colored circles) from Whitehouse, Bentley, Milne, et al. (2012) are plotted using the same color scale. The radius of the circle at each GPS site is inversely proportional to the GPS uncertainty at that site. In (c–d), these maps are compared with the uplift rates maps obtained by coupling both ice loading histories with an SGVEM: (c) displays the difference between (a) and the modeled uplift rates reproduced in Whitehouse, Bentley, Milne, et al. (2012) and (d) displays the difference between (b) and the modeled uplift rates reproduced in Argus et al. (2014).

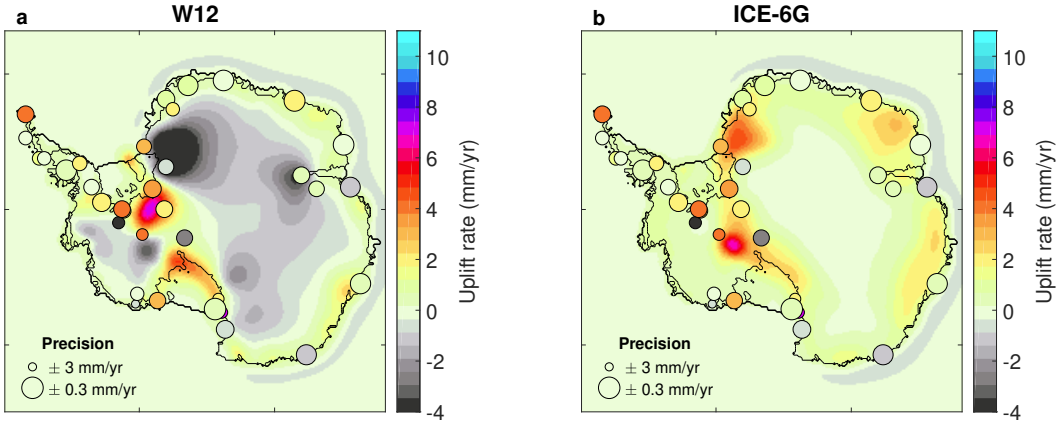

Figure 4. Ensemble mean uplift rate maps reproduced with (a) W12 and (b) ICE-6G ice-loading histories. GPS observations of present-day uplift rates (colored circles) from Whitehouse, Bentley, Milne, et al. (2012) are plotted using the same color scale. The radius of the circle at each GPS site is inversely proportional to the GPS uncertainty at that site.

$$\mathrm{WRMS} = \sqrt{\frac{\sum_{i=1}^{N_{\mathrm{obs}}} (p_i - \mathrm{obs}_i)^2 w_i}{\sum_{i=1}^{N_{\mathrm{obs}}} w_i}}, \tag{10}$$

where N_{obs} is the number of observation points, p_i and obs_i are the predicted and observed uplift rates at observation site i, respectively, and $w_i = 1/\sigma_i^2$ is the weight at observation site i, where σ_i is the standard deviation given by $\sigma_i^2 = \left(\sigma_i^{\mathrm{GPS}}\right)^2 + \left(\sigma_i^{\mathrm{ELRA}}\right)^2$, with σ_i^{GPS} and σ_i^{ELRA} the standard deviations of the observed and predicted uplift rates, respectively, allowing to consider the GPS uncertainty at each site as well as the "model uncertainties" (Whitehouse, Bentley, Milne, et al., 2012). Note that σ_i^{ELRA} is estimated as the standard deviation of the predicted uplift rates of our 2000 Monte Carlo samples. Even though we neglect the part of the GIA signal associated with the depth-variability of the Earth structure, the 2000 spatially-varying solid-Earth configurations of our ensemble provide a better fit to observations of present-day uplift rates (lower WRMS errors) than if the ELRA model is driven by the W12 and ICE-6G ice-loading histories using spatially-uniform ELRA parameters (See Supporting Information Figures S2–S3). This behavior is in agreement with van der Wal et al. (2015), who show that using an Earth rheology that considers the weak Earth structure of West Antarctica provides maps of predicted uplift rates consistent with GPS observations of uplift rates (Whitehouse, Bentley, Milne, et al., 2012), and with a better fit to observations than spatially-uniform ELRA models.

In order to assess the importance of GIA feedbacks on the response of the AIS, we compare grounded-ice volume projections for four RCP scenarios assuming (i) a fixed geoid and a rigid Earth, (ii) gravitational geoid changes and a rigid Earth, and (iii) gravitational geoid changes and solid-Earth changes (Figure 5). In accordance with Gomez et al. (2015), who use a global SGVEM and consider gravitationally-consistent sea-level changes, we show a stabilizing influence of gravitationally-consistent geoid changes. Globally, under all RCP scenarios, including geoid changes leads to a decrease in mass loss as compared with a fixed geoid and rigid-Earth experiment (the exception observed under RCP 4.5 between 3000 and 5000 CE is examined in the discussion section). The inclusion of solid-Earth deformation in addition to geoid changes further stabilizes the AIS and reduces mass loss. Contrary to Gomez et al. (2015), we find that bedrock adjust-

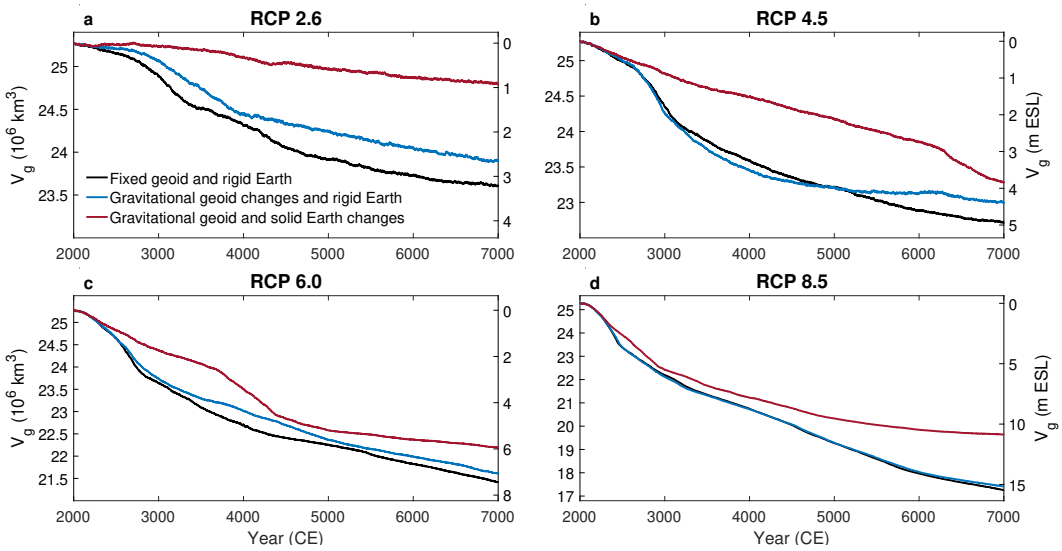

Figure 5. Impact of gravitationally-consistent sea level and solid-Earth changes on Antarctic grounded-ice volume (V_g) projections under RCP 2.6 (a), 4.5 (b), 6.0 (c), and 8.5 (d). Median values of the ELRA parameters are considered ($\tau_W = 70.71$ yr; $\tau_E = 7071$ yr; $D_W = 10^{23}$ N m; $D_E = 5\text{x}10^{24}$ N m). The right ordinate gives an approximation of the equivalent sea-level contribution computed following Goelzer et al. (2020) and considered as a linear function of grounded-ice volume.

ment tends to dominate the stabilizing effect of GIA feedbacks, although the magnitude of the influence varies through the simulations and with the climate forcing applied. For example, under RCP 4.5, the model that only incorporates geoid changes yields, after 5000 years, ∼50% of the decrease in grounded ice mass loss predicted by the simulation that includes both gravitational and deformational effects; this proportion decreases to about 6% under RCP 8.5 (see also Supporting Information Figure S4). The relative importance of self-gravitation depends on many factors, including the strength of the climate forcing, viscoelastic Earth structure, bedrock configuration, and the rate and spatial pattern of ice loss (Gomez et al., 2015). We attribute the difference between our results and those of Gomez et al. (2015) to the fact that we consider a spatially-varying Earth structure with a low viscosity beneath West Antarctica while Gomez et al. (2015) adopt a continent-wide high viscosity Earth model. In a complementary study that explores the potential for rapid viscoelastic deformation to stabilize Pine Island glacier on centennial timescales, Kachuck et al. (2020) show that instantaneous components of the solid-Earth response (purely elastic deformations, geoid perturbations) provide less stability than the viscoelastic response. This may be explained by the fact that when the solid-Earth response is sufficiently rapid, the geoid perturbation due to ice mass loss is rapidly counterbalanced by bed uplift. The proposed elementary GIA model is thus shown to be capable of reproducing the stabilizing effect of GIA feedbacks highlighted in previous studies (Gomez et al., 2012, 2013; Adhikari et al., 2014; Gomez et al., 2015; Konrad et al., 2015, 2016; Larour et al., 2019; Kachuck et al., 2020).

2.3 Probabilistic Assessment Methods

We perform a probabilistic assessment of the impact of uncertainties in solid-Earth rheological properties on the response of the AIS for each RCP scenario. We consider the four parameters, τ_{W}, τ_{E}, D_{W}, and D_{E} to be uncertain parameters with uncertainty ranges given in Table 1. We represent these four uncertain parameters as independent

random variables and assume the marginal probability distributions to follow a log-uniform distribution. The choice of log-uniform distributions is relevant for uncertain parameters that cover a large range of values (several orders of magnitude) and for which the only available information is the uncertainty ranges (Pueyo, 2012). We determine probabilistic projections of the grounded-ice volume, marginal probabilities of being ungrounded, as well as Sobol sensitivity indices using Monte Carlo estimation (Robert & Casella, 2013) with 2000 (independent and identically distributed) samples of the uncertain parameters. Sobol indices rely on the decomposition of the variance of the projections as a sum of contributions from each uncertain parameter taken individually, as well as an interaction term (Saltelli et al., 2008; Bulthuis et al., 2019). A value of 1 indicates that the entire variance of the projections is explained by this sole uncertain parameter and a value of 0 indicates that the uncertain parameter has no impact on the projection uncertainty. Due to the overlap between the uncertainty ranges and the assumption of statistical independence between the parameters, not all Monte Carlo ensemble members (strictly) correspond to *plausible* solid-Earth configurations for Antarctica. By the latter, we mean an Earth structure that is representative of geophysical evidence (e.g., Morelli & Danesi, 2004; An et al., 2015; Lloyd et al., 2020) and therefore characterized by a more rigid Earth structure beneath East Antarctica than West Antarctica (i.e., $D_E > D_W$ and $\tau_E > \tau_W$). However, *non-plausible* Monte Carlo ensemble members only represent 5% of all samples (hence a small region of the parameter space) and their presence does not affect the overall behavior of the ensemble (see Supporting Information Figure S5). Let us note that our methodology can readily be extended to dependent parameters except for the computation of Sobol indices whose definition relies on the assumption of statistical independence between the parameters. For each of the 2000 Monte Carlo samples, we estimate the change in grounded-ice volume from the ice-sheet model and we determine the median values and quantiles of the projections as the sample medians and quantiles. For this purpose, 2000 samples are sufficient to ensure reasonable convergence of the Monte Carlo estimates. Probability density functions of the responses are estimated through kernel density estimation (Scott, 2015).

3 Results

Figure 6 shows probabilistic projections of Antarctic grounded-ice volume for the four RCP scenarios. As expected, we observe an increase of AIS mass loss as time evolves and warming increases. Apart from RCP 2.6, all scenarios lead to multi-metre sea-level rise in agreement with previous studies (Golledge et al., 2015; Bulthuis et al., 2019; Garbe et al., 2020). In Figure 7, these probabilistic projections are compared to (i) a forced run without bedrock and sea-level adjustments (NOGIA, relative sea level remains constant) and (ii) a run using the ELRA model with fixed uniform reference parameters commonly used in the literature (UNIBED; $\tau = 3000$ yr and $D = 10^{25}$ N m; Le Meur & Huybrechts, 1996). For all scenarios, the NOGIA curve lies close to the lower limit of the ensemble (Figures 7a–d) demonstrating that the inclusion of GIA has a stabilizing effect on mass loss. Simulations in which GIA feedbacks lead to an increased mass loss as compared to the NOGIA experiment (as can be observed under RCP 2.6 and 4.5, Figures 7a–b) may be explained by forebulge effects (see discussion section). For RCP 2.6, 4.5, 6.0 (before $\sim$3500 CE), and 8.5 (before $\sim$3000 CE), the UNIBED experiment is also close to this lower limit while for RCP 8.5 on longer timescales, the ensemble generally produces more mass loss than the UNIBED experiment. The reasons behind this behavior may be enlightened by Figure 8, which shows that our ensemble results for West and East Antarctica evolve very differently to the UNIBED case. Specifically, the inclusion of weak Earth structure beneath West Antarctica results in less mass loss compared with the UNIBED case (Figure 8a–d), while at long timescales and for strong forcing (Figure 8h), central estimates of mass loss from East Antarctica (assuming a relatively strong Earth structure) are greater than the UNIBED case.

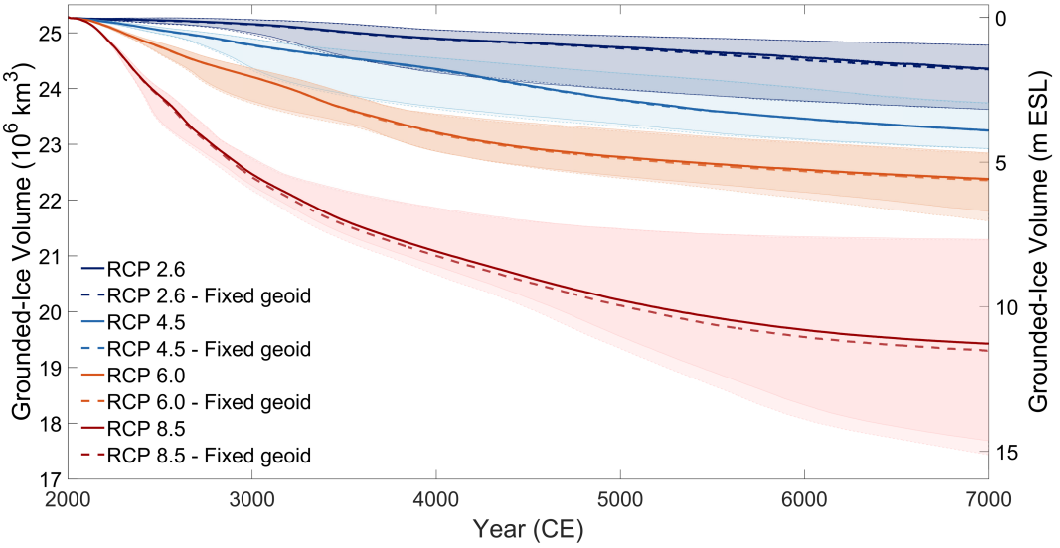

Figure 6. Probabilistic projections of the grounded-ice volume under different RCP scenarios: evolution of the medians and 5–95% probability intervals. Solid lines represent the median projections while shaded areas are the 5–95% probability intervals that represent the uncertainty in grounded-ice volume projections due to uncertainty in ELRA parameters. Dashed lines represent probabilistic projections for which only bedrock adjustment is considered, i.e., without including gravitationally-consistent sea-level changes. The right ordinate gives an approximation of the equivalent sea-level (ESL) contribution computed following Goelzer et al. (2020) and considered as a linear function of grounded-ice volume.

The spatial distribution of mass loss at the end of the projections is shown in Figure 9 (as a comparison, grounding-line migration of the UNIBED experiments is displayed in Supporting Information Figure S6). Grounded-ice loss follows a pathway of progressive collapse of the WAIS with increasing warming scenario, followed by a retreat in the Wilkes and Aurora basins in the EAIS for RCP 6.0 and 8.5 on longer timescales. For weak warming scenarios (RCP 2.6), a complete WAIS collapse has a low probability, even after 5000 years of simulations: mass loss is concentrated in the Amundsen Sea sector (Pine Island and Thwaites glaciers) and in Siple Coast, but rarely leads to a complete MISI. Under RCP 8.5, a complete WAIS collapse in the first millennium has a very high probability while on longer timescales the additional mass loss arising from the EAIS is much more uncertain, leading to a wide spread in projections of AIS sea-level contribution (ranging between 7.5 and 15 m at 7000 CE, see Figures 6 and 7d). The probability of ice loss by 7000 CE in Aurora basin is much lower than in Wilkes basin (Figure 9d), suggesting that a complete collapse of Wilkes basin is triggered almost independently of the values of the rheological parameters, while the retreat in Aurora basin is strongly dependent on the solid-Earth structure. This increases the uncertainty in the distribution, making it more skewed or even bimodal (see Figure 10). Naturally, the results presented here also depend on the initialization procedure (Cornford et al., 2015; Seroussi et al., 2019), even though the influence of initialization decreases with increasing climate forcing. As a comparison, the behavior of control simulations under constant present-day climate is displayed in Supporting Information (Figures S7–S9). Due to imposed present-day melt rates as a representation of present-day forcing, control simulations display a retreat in the Amundsen Sea Sector.

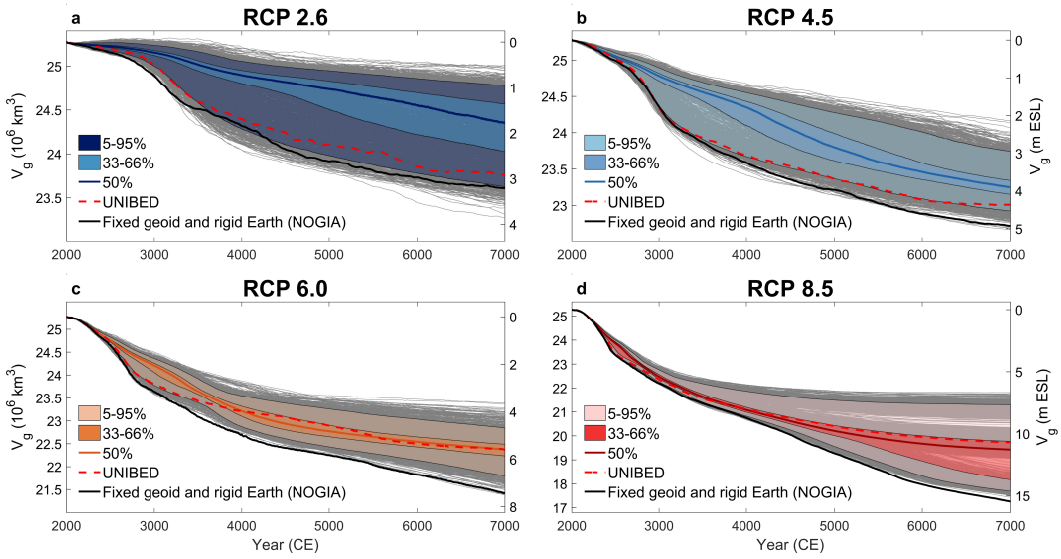

Figure 7. Antarctic grounded-ice volume (V_g) projections considering uncertainty in Antarctic viscoelastic properties under RCP 2.6 (a), 4.5 (b), 6.0 (c), and 8.5 (d). Colored solid lines are the median projections while shaded areas are the 33–66% and 5–95% probability intervals that represent the uncertainty in grounded-ice volume projections due to uncertainty in ELRA parameters. Black lines correspond to control simulations in which both bedrock and sea-level adjustments are not included (NOGIA). Dashed red lines correspond to simulations with uniform reference ELRA parameters (UNIBED) taken from Le Meur and Huybrechts (1996). Grey lines represent time series of Antarctic grounded-ice volume for the ensemble of 2000 Monte Carlo simulations. The right ordinate gives an approximation of the equivalent sea-level contribution computed following Goelzer et al. (2020) and considered as a linear function of V_g.

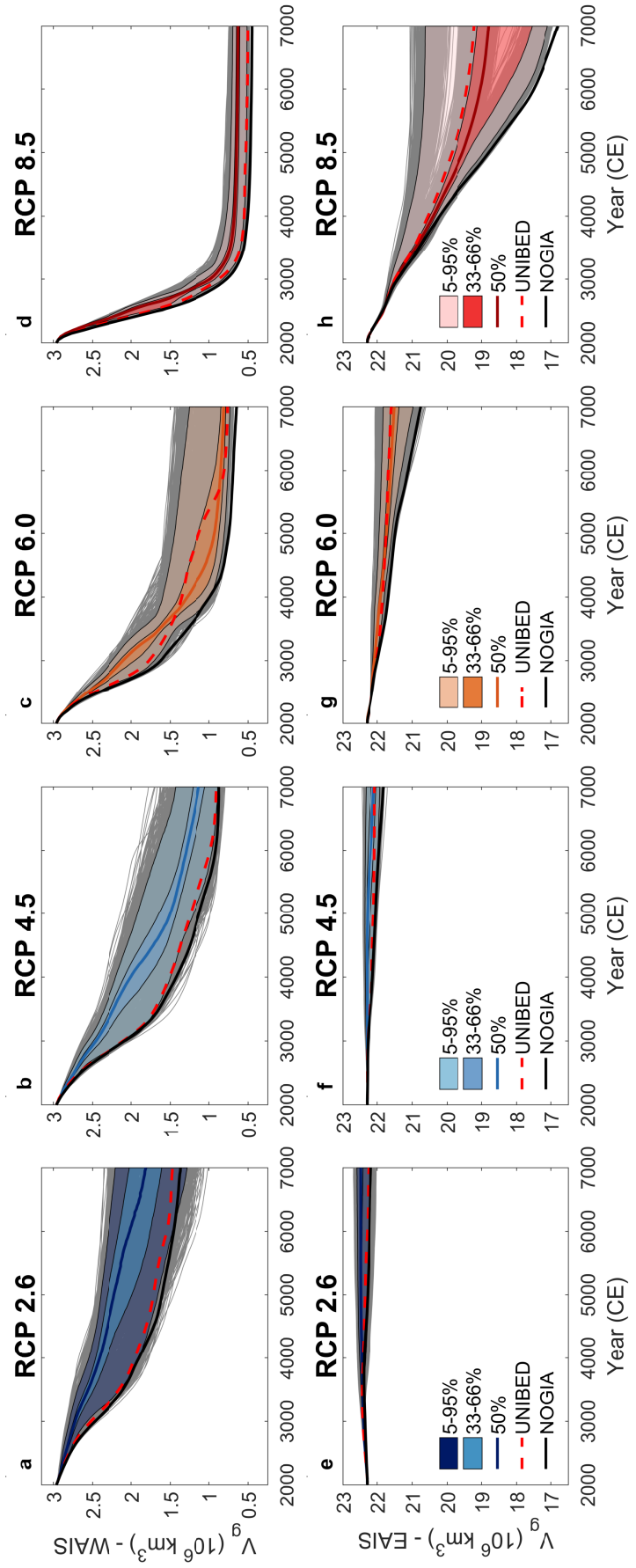

Figure 8. West (a–d) and East (e–h) Antarctic grounded-ice volume projections considering uncertainty in Antarctic viscoelastic properties under RCP 2.6 (a, e), 4.5 (b, f), 6.0 (c, g), and 8.5 (d, h). Colored solid lines are the median projections while shaded areas are the 33–66% and 5–95% probability intervals that represent the uncertainty in grounded-ice volume (V_g) projections due to uncertainty in ELRA parameters. Black lines in (a–h) correspond to control simulations in which both bedrock and sea-level adjustments are not included (NOGIA). Dashed red lines correspond to simulations with uniform reference ELRA parameters (UNIBED) taken from Le Meur and Huybrechts (1996).

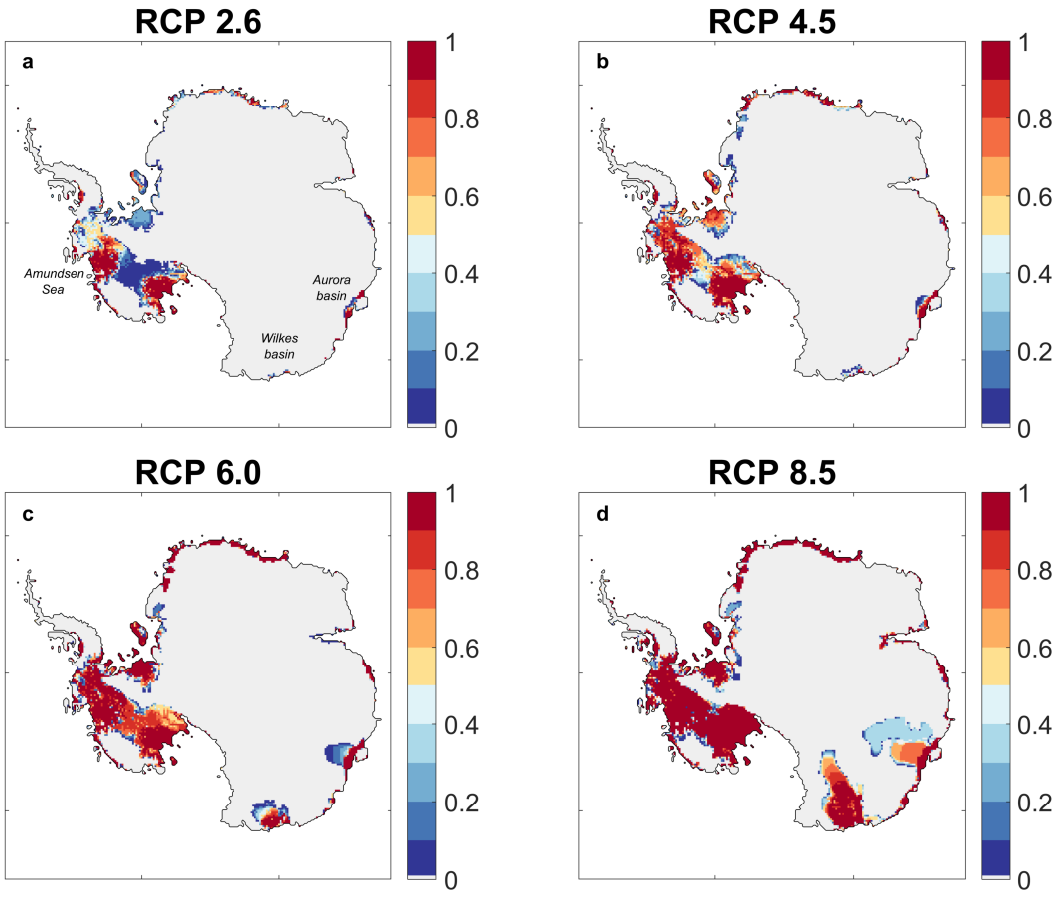

Figure 9. Marginal probability of being ungrounded under the four RCP scenarios at 7000 CE. For each RCP scenario, the marginal probability of being ungrounded at a given point is computed using Monte Carlo estimation with the ensemble of 2000 simulations. Results are for RCP 2.6 (a), 4.5 (b), 6.0 (c), and 8.5 (d). Grey regions correspond to locations where there is a 0% probability of being ungrounded. Present-day grounding lines are shown in black.

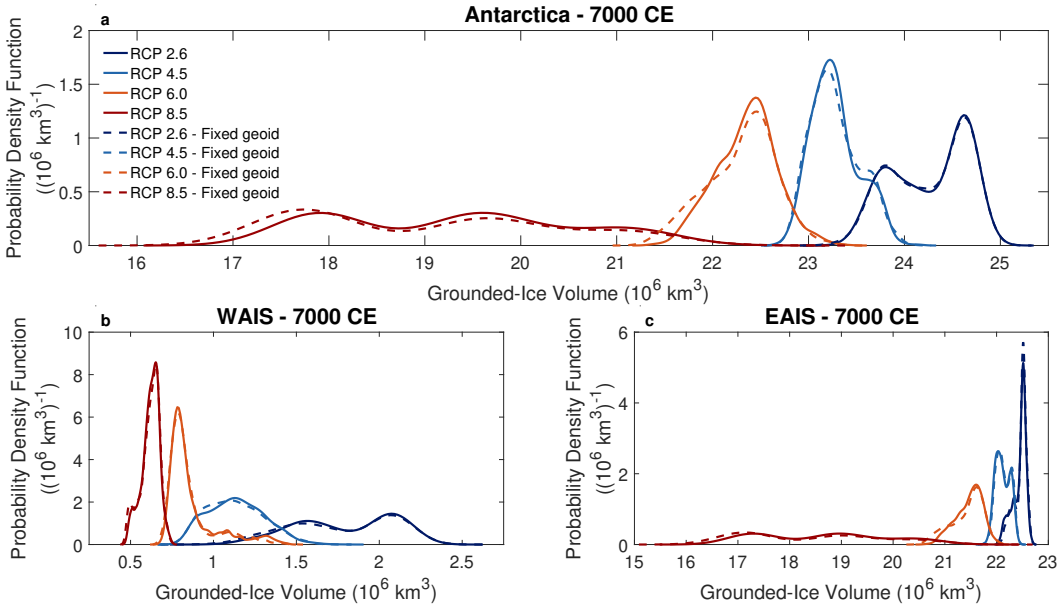

Figure 10. Probability density functions for the Antarctic (a), West Antarctic (b) and East Antarctic (c) grounded-ice volumes at the end of the 5000-yr simulations (7000 CE) under the four RCP scenarios. Dashed lines represent probability density functions for simulations in which only bedrock adjustment is considered, i.e., excluding gravitationally-consistent sea-level changes.

The delay in WAIS retreat (and collapse for higher RCPs) of our ensemble as compared to the UNIBED and NOGIA experiments (Figures 7 and 8) is easily explained by the fact that a lower upper-mantle viscosity (smaller τ_W) and, to a lesser extent, a thinner lithosphere thickness (lower D_W) lead to faster and more localized uplift rates in areas of mass loss, reducing the water depth (relative sea level) in the vicinity of the grounding line. This leads to a more stable grounding-line position, hence counteracting MISI and lowering projections of future mass loss, as shown by previous studies (Gomez et al., 2013; Adhikari et al., 2014; Gomez et al., 2015; Konrad et al., 2015, 2016). As warming and time increase, the stabilizing effect of GIA feedbacks on projections of future WAIS mass loss decreases: the median of the ensemble gets closer to the UNIBED scenario (Figures 8a–d). Under RCP 8.5, WAIS collapse occurs rapidly (after about 1000 years, Figure 8d) because the climate forcing overrides the GIA stabilization, even for the weak Earth models used in this region. As WAIS collapse nears completion, grounding-line retreat is triggered in EAIS marine basins (from RCP 6.0, essentially under RCP 8.5; see Figures 8 and 9), leading to a more pronounced grounding-line retreat (greater ice loss in the ensemble) as compared with the UNIBED experiment. The reason for this is a generally higher regional upper-mantle viscosity (greater τ_E) compared to the UNIBED experiment, leading to lower uplift rates and hence a less stable grounding-line position. The weaker stabilizing effect of high τ_E values occurs despite lower D_E values than in the UNIBED experiment.

The above observations are corroborated by the evolution of Sobol sensitivity indices for the change in grounded-ice volume under the different RCP scenarios (Figures 11a–d). Sobol indices decompose the dispersion (variance) of the grounded-ice volume into fractions which can be attributed to each uncertain parameter. They can be interpreted as measures of the sensitivity of the grounded-ice volume to the input ELRA parameters. For all RCPs, τ_W is a highly influential parameter in controlling the ice-sheet response. Its dominating impact shifts from the whole time period (RCP 2.6) towards the

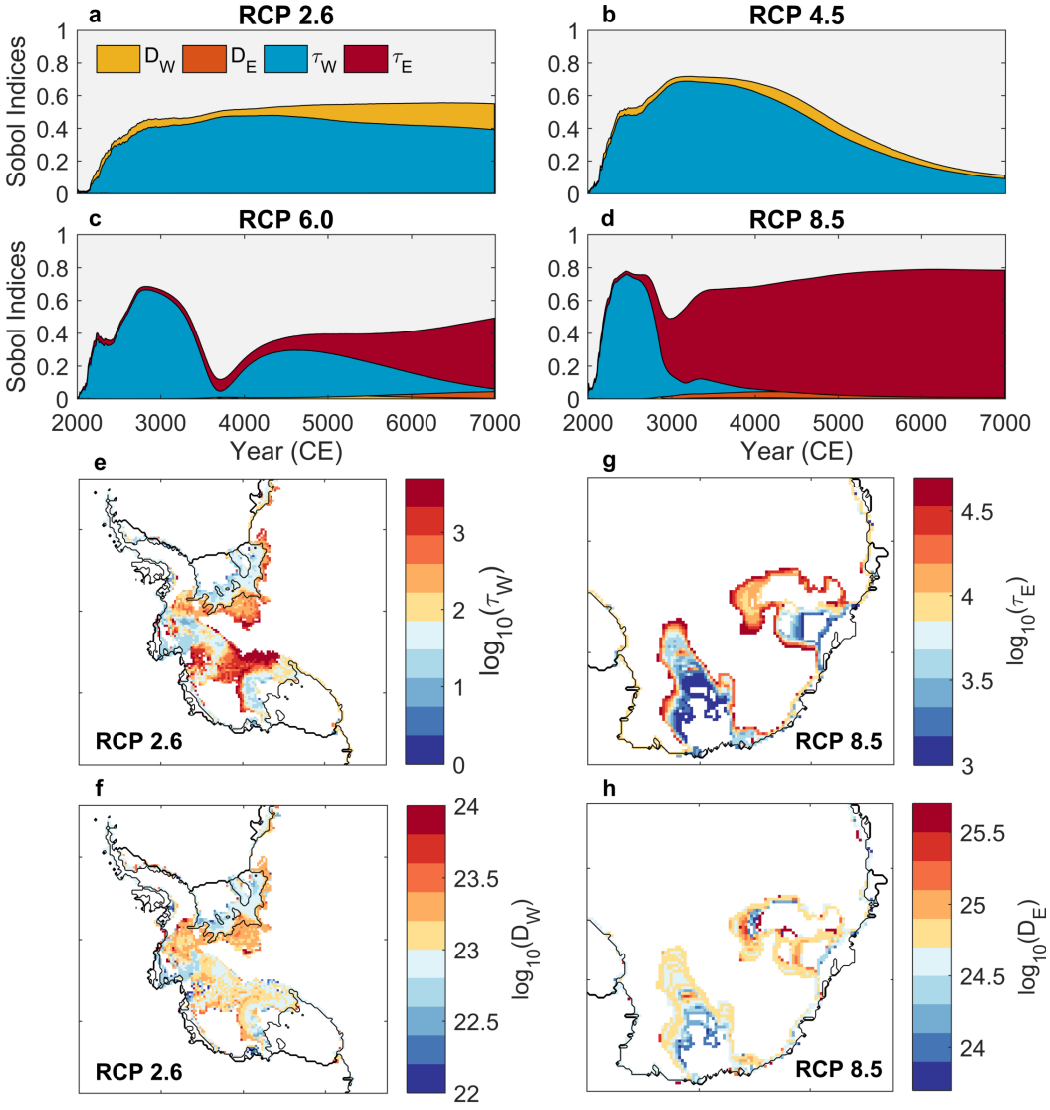

Figure 11. Sensitivity of future Antarctic ice sheet behavior to ELRA solid-Earth parameters. Evolution of Sobol sensitivity indices for the grounded-ice volume under RCP 2.6 (a), 4.5 (b), 6.0 (c), and 8.5 (d). The Sobol index of a given uncertain parameter represents the fraction of the variance of the projections explained as stemming from this sole uncertain parameter. A value of 1 indicates that the entire variance of the projections is explained by this sole uncertain parameter and a value of 0 indicates that the uncertain parameter has no impact on the projection uncertainty. Grey area corresponds to the interaction index, which represents the influence of the interaction between the parameters on the projection uncertainty. Sensitivity of future grounding-line retreat to solid-Earth structure is highlighted in Figures (e)–(h), where the position of the grounding line at the end of the 5000-yr simulation for the 2000 Monte Carlo simulations is color-coded according to the mean value of one of the ELRA parameters. Figures (e)–(h) show the sensitivity of final grounding-line position under RCP 2.6 to τ_W (e) and D_W (f) and under RCP 8.5 to τ_E (g) and D_E (h).

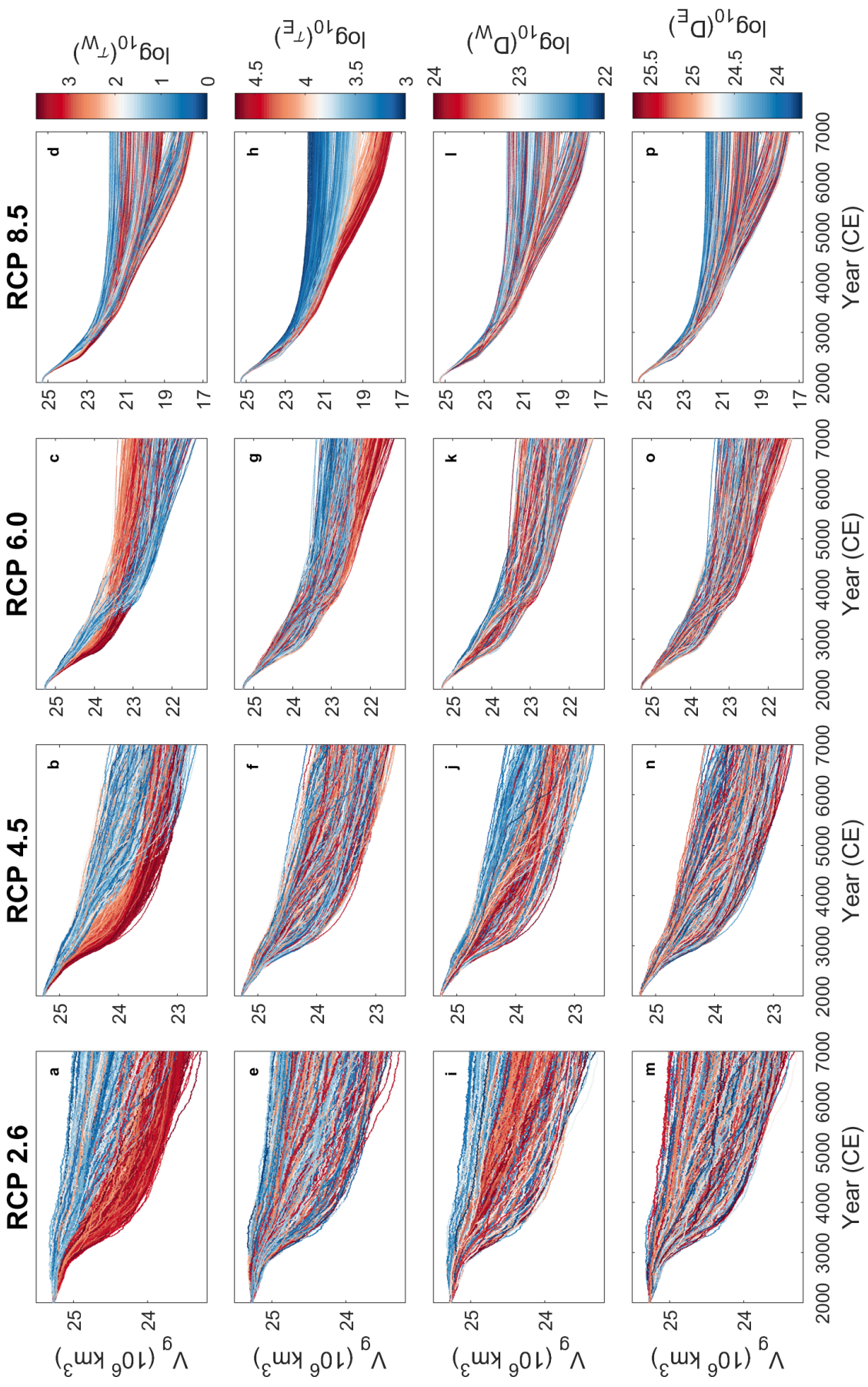

Figure 12. Antarctic grounded-ice volume projections (V_g) under RCP 2.6 (a, e, i, m), 4.5 (b, f, j, n), 6.0 (c, g, k, o), and 8.5 (d, h, l, p) for 2000 Monte Carlo samples from the parameter space. Time-series of the ensemble are color-coded by values of (a–d) $\log_{10}(\tau_W)$, (e–h) $\log_{10}(\tau_E)$, (i–l) $\log_{10}(D_W)$, and (m–p) $\log_{10}(D_E)$. Units for D_W and D_E are N m and units for τ_W and τ_E are years.

first 1000 years (RCP 8.5) with increasing RCP scenario, demonstrating its control on the stability of the WAIS. The second most influential parameter is τ_E; however its influence is limited to the longer timescales of RCP 6.0 and mostly 8.5. Indeed, the prevailing effect of τ_E only appears once WAIS collapse has occurred and grounding-line retreat has begun in EAIS marine basins (also shown by Figure 12). The influence of τ_E increases as EAIS retreat progresses. From the Sobol indices, it is clear that spatial variability in the lithosphere thickness is less important in controlling the response of both ice sheets than spatial variability in upper-mantle viscosity. The WAIS flexural rigidity D_W does play a role, although less pronounced, and its contribution to the dispersion of the distribution progressively decreases as the collapse of the WAIS advances under higher RCPs. Sobol indices therefore show a dominant dependence of the projections on the relaxation time, with a two-step behavior as climate forcing increases. Note that when the sum of the Sobol indices is not equal to 1, the remaining index stems from the interactions between the parameters.

The dominant effect of the mantle relaxation time compared to the lithosphere flexural rigidity can also be observed in Figures 11e–h, which illustrate the influence of solid-Earth structure on grounding-line retreat, and Figure 12, which shows the influence of solid-Earth structure on projections of future AIS mass loss. Under RCP 2.6 and 4.5, WAIS collapse occurs only for the more rigid Earth structures (Figure 9a–b and 11e, f). Weak Earth structures thus seem to reduce or delay grounding-line retreat. Note that this effect is more pronounced for the Ross and Weddell Sea Embayments than for other basins (see Supporting information Figures S10–S14) because of their relatively flat reverse bed slopes (Adhikari et al., 2014). Mass gain may even be observed in the Weddell Sea Embayment for the weakest Earth structures. Under stronger climate forcings (RCP 6.0 and 8.5), the weak Earth structure in WAIS can no longer prevent a collapse. In addition, grounding-line retreat is triggered in EAIS. More specifically, under RCP 8.5, a significant retreat of the grounding line occurs in the marine basins of Wilkes and Aurora only for stiffer solid-Earth structures (Figures 11g–h), implying that the latter reenforce retreat due to the prediction of greater water depths at the grounding line compared to weaker solid-Earth configurations. Again, a difference in sensitivity between the two EAIS marine basins is observed: in the Aurora basin (where the relaxation time of the asthenosphere strongly determines stable grounding-line locations), weak solid Earth configurations are still able to (almost) prevent grounding-line retreat while collapse of a large portion of the Wilkes basin seems to be engaged whatever the regional viscoelastic properties considered. This can also be observed in Supporting information Figures S10–S14 which display the influence of Earth structure on the timing of the initiation of collapse for different sectors of the AIS. The influence of Earth structure on grounding-line retreat progressively decreases with increasing forcing in the main West Antarctic basins. GIA feedbacks have very little influence under RCP 8.5 (especially in the Amundsen Sea Embayment) whereas grounding-line retreat may be delayed by several thousands of years for some Earth models under weaker forcing. In contrast, an increasing influence of Earth structure on the timing of retreat is observed in the Wilkes and Aurora basins as the forcing increases.

In order to assess the influence of gravitational effects on the AIS response, we also represented in Figures 6 and 10 projections for an ensemble of 2000 Monte Carlo simulations without gravitational effects, i.e., with a fixed geoid. These figures show that considering gravitationally-consistent geoid changes stabilizes the AIS to a greater extent than when only bedrock adjustment is considered, especially under RCP 8.5. Indeed, the stabilizing effect of local sea-level adjustment increases with the amount of ice mass change involved (see Supporting Information Figures S15-S18). Conversely, when grounding-line retreat is triggered in the EAIS, the stabilizing effect of the local perturbation to the geoid due to ice sheet mass loss is less efficiently counterbalanced by the gravitational attraction of rising mantle material (see Supporting Information Fig. S4) because of the slower response of the solid Earth in this region. Note that considering

gravitational effects can also lead to increased mass loss (as can be observed in Figure 5), potential reasons for this are discussed in section 4.

4 Discussion

We analyzed the multi-millennial sensitivity of the AIS to near-field relative sea-level changes due to GIA, with a specific focus on (i) viscous bedrock changes induced by a weak solid-Earth response in West Antarctica, (ii) the contrast with the strong-Earth response in East Antarctica, and (iii) the effect of changes in geoid height. With very few exceptions (e.g., Gomez et al., 2018), ice-sheet models are typically coupled to Earth deformation models that consider spatially-homogeneous solid-Earth properties, whatever their level of complexity: from simple ELRA models (e.g., Pollard et al., 2015; DeConto & Pollard, 2016; Pattyn, 2017), to intermediate Earth-deformation models that incorporate mode-dependent relaxation times and elastic deformation (e.g., based on Bueler et al. (2007) such as in Golledge et al., 2015; Kingslake et al., 2018; Garbe et al., 2020), to full SGVEMs (e.g., Konrad et al., 2015; Gomez et al., 2015; de Boer et al., 2017; Pollard et al., 2017). However, this homogeneity is not representative of the Antarctic continent, which is characterized by a complex viscoelastic setting, with the WAIS underlain by a rift system while the EAIS lies upon an old thick craton (An et al., 2015). This translates into strong lateral variations in lithosphere thickness and mantle viscosity between the two regions, with a thick lithosphere and high mantle viscosity characterizing East Antarctica, and in contrast, a thin lithosphere and low mantle viscosity beneath West Antarctica (Morelli & Danesi, 2004; Lloyd et al., 2020; Pappa et al., 2019). In addition to this West-East dichotomy, strong viscoelastic heterogeneities (sometimes by several orders of magnitude across relatively short spatial scales) exist within the East and West Antarctic regions (An et al., 2015; Chen et al., 2018; Lloyd et al., 2020). Here, we use a simple ELRA model adapted to account for lateral variations in viscoelastic properties together with an approximation for local geoid changes due to mass changes. The use of an ELRA model remains an approximation to a global SGVEM (Konrad et al., 2014, 2016), but given the uncertainties associated with Antarctic solid-Earth properties (lithosphere thickness and upper-mantle viscosity), we believe that the impact of structural uncertainty in GIA models is smaller than the impact of parametric uncertainty. Moreover, ice-sheet models are typically run assuming that the sea surface adjacent to an ice sheet is uniform, either remaining constant or tracking global mean sea-level changes, which is not realistic. In this framework, our elementary and computationally-efficient GIA model represents a somewhat comprehensive model of local relative sea-level changes (Figure 1), allowing to consider the extent of these viscoelastic uncertainties over a long-term probabilistic assessment (hardly envisageable with SGVEMs considering a 3-D Earth rheology) while capturing the essential features and processes influencing AIS grounding-line stability. However, it is important to mention that in order to be able to study lateral variability in Antarctic Earth structure, the depth variability of the Earth structure within the upper mantle (which may be important) has been ignored, as it is not captured by the ELRA model.

Our results support recent studies (Gomez et al., 2015; Konrad et al., 2015) suggesting that ice–Earth interactions are not expected to substantially slow down the global mean sea-level rise contribution from the AIS over the 21st century, but that these processes could become important on multicentennial and millennial timescales. Indeed, during the first few hundred years, projections from the ensemble show limited differences for different solid-Earth configurations (Figures 7a–d), implying that the ice loss over this period is mainly governed by climate forcing. On longer timescales, however, the future behavior of the AIS becomes significantly influenced by its solid-Earth structure. Similar to Konrad et al. (2015), we show that under limited forcing (RCP 2.6 and 4.5), weak solid-Earth configurations are able to significantly delay (sometimes by several thousands of years) grounding-line retreat or even prevent WAIS collapse. However, the lat-

ter cannot be avoided as climate forcing increases (Figure 9). Under strong RCP 8.5, significant divergence in ice mass loss appears after $\sim$1000 years for the different solid-Earth structures from the ensemble. At 7000 CE, the 5-95% probability interval corresponds to more than 7 meters of sea-level rise (it is less than 2 m for RCPs 2.6, 4.5 and 6.0), which means that the sea-level contribution arising from the AIS may be doubled depending on the local viscoelastic properties. This uncertainty arises from deviations in behavior in the EAIS marine basins where grounding-line retreat is triggered by climate forcing (in agreement with results from Pollard et al., 2017). Differences between the various projections essentially occur in the marine basins of Wilkes and Aurora (which are together responsible for more than 60% of the uncertainty in AIS mass loss at 7000 CE under RCP 8.5): on long-term timescales, Wilkes basin is more sensitive to the climate forcing, leading to a significant grounding-line retreat independent of the solid-Earth structure, while the sensitivity of Aurora basin is strongly GIA-dependent (Supporting Information Figure S14). This difference in behavior between these two basins may probably be explained by the contrasting topographic features characterizing both areas, with retrograde slopes observed in Wilkes subglacial basin but stabilizing slopes, deep troughs and pinning points observed in Aurora basin (Aitken et al., 2016; Morlighem et al., 2019).

Previous studies evaluating the uncertainty in future Antarctic behavior (e.g. DeConto & Pollard, 2016; Bulthuis et al., 2019) considered either uniform solid-Earth properties, or spatially-varying configurations but with smaller uncertainty ranges for the solid-Earth parameters. Bulthuis et al. (2019) already suggested that relaxation times beneath WAIS that vary widely from a few decades to a few millennia may exert a significant influence on the AIS response. Here, we show that uncertainties on millennial timescales may be larger than previously thought, mainly arising from the EAIS.

One of the goals of this study was to compare the projections of our ensemble (considering spatially-varying solid-Earth structures) to characteristic projections (Figures 7 and 8), more specifically to (i) projections neglecting GIA feedbacks and (ii) projections considering a homogeneous average solid-Earth structure. In agreement with other work (e.g., Konrad et al., 2015; Gomez et al., 2015), our results show that (i) adding GIA feedbacks has a stabilizing effect (with a higher impact for weaker solid-Earth structures i.e., low viscosity and, to a lesser extent, thin lithosphere; Konrad et al., 2015, 2016) relative to projections that do not include them, and (ii) incorporating the low viscosities characterizing West Antarctica makes a difference relative to those projections that assume a homogeneous average structure. More specifically, the latter overestimate the sea-level contribution from the AIS for timescales shorter than 1000 years (Figures 7a–d). By 3000 CE, AIS mass loss estimated by the median projections of our ensemble is reduced by about 50% under both RCP 2.6 and 4.5, 30% under RCP 6.0 and nearly 5% under RCP 8.5 as compared to the UNIBED projections. In contrast, our results also show that for longer timescales and at sufficient climate forcing, i.e., when grounding-line retreat in East Antarctica becomes significant (only after WAIS collapse, because the EAIS basins are protected by narrower and shallower sills; Pollard et al., 2015), future projections may underestimate the contribution from the EAIS if they do not account for the higher than average viscosity of the region (Figures 7d and 8h). By the end of the 5000-yr simulations, AIS mass loss may be underestimated by up to almost 40% (5-95% probability interval) as compared to UNIBED due to underestimation of EAIS mass loss.

Even though our results generally document the stabilizing effect of GIA feedbacks, we have identified two distinct GIA-related behaviors that may induce an increase in mass loss relative to projections omitting GIA feedbacks. One class of behavior, represented by the lowest grey lines in Fig. 7a is thought to be related to the migration of topographic forebulges during bedrock adjustment, which causes local crustal motions (and slopes) to change sign (Adhikari et al., 2014), thereby generating configurations that are more vulnerable to instability (Kachuck et al., 2020). Note however that forebulges are a com-

ponent of our GIA model that are simulated the least accurately (see section 2.2.3). The other class of behavior, represented in Fig. 5b, is seen when non-linear feedbacks between complex topography and gravitationally-consistent geoid changes lead to unstable grounding-line retreat. More specifically, such behavior may be observed in response to the following series of events: (i) the ice sheet simulated by the model including geoid changes locally re-advances, probably encouraged by the lower local sea level arising from the gravity effect of the mass loss occurring in the area and the formation of ice rises, (ii) this local ice advance (increase in ice mass) triggers an increase in local sea level, which leads to (iii) an increase in grounding-line flux and (iv) upstream thinning beyond the initial configuration, such that (v) subsequent retreat causes the grounding line to end up in an unstable position. Such non-linear behavior depends on the details of the topography and a specific combination of events such that a small oscillation in ice mass is amplified and the ice sheet ends up in an unstable state.

The main limitation of our approach lies in its sensitivity to the defined viscoelastic setting and parameter space, as we adopted rather large uncertainty ranges for the ELRA parameters. More realistic probabilistic distribution of the uncertain parameters could be inferred using statistical (inverse) methods such as Bayesian inference (e.g., Caron et al., 2018) constrained with observed uplift rates. While this is out of the scope of this study, we believe that such an analysis would constitute an interesting future work. However, note that this inference would intrinsically be biased by the fact that existing ice loading histories, i.e., ICE-6G (Argus et al., 2014) and W12 (Whitehouse, Bentley, & Le Brocq, 2012; Whitehouse, Bentley, Milne, et al., 2012), do not account for post-2 ka BP ice mass change and were tuned to fit geological and geodetic observations by assuming a laterally-homogeneous solid Earth (van der Wal et al., 2015; Hay et al., 2017). In addition, it is important to underline that we made the choice to ignore intra-regional viscoelastic heterogeneities in order to focus on the West–East dichotomy. As stated by Nield et al. (2018), including lateral variations in solid-Earth rheology at least to the level of considering West and East Antarctica separately is important. However, future work should focus on taking these intra-regional heterogeneities into account. Indeed, some of the most extreme low viscosities are inferred under the modern Thwaites and Pine Island Glacier regions of the WAIS (Barletta et al., 2018; Lloyd et al., 2020), which are currently responsible for the largest contribution of Antarctica to global sea level rise (Rignot et al., 2019). Accounting for the full lateral variability of Antarctic Earth structure would likely significantly delay projections of mass loss in those areas where unstable grounding-line retreat is already underway (Favier et al., 2014; Joughin et al., 2014; Scambos et al., 2017). According to Barletta et al. (2018), the low viscosity structure under the Amundsen Sea Embayment might produce a deformation large enough and early enough in the deglaciation phase to prevent the complete collapse of the WAIS, even under strong climate forcing. Note, however, that the projections of our ensemble that are characterized by the weaker WAIS solid-Earth configurations (hence also applied over the Amundsen Sea Embayment region) still display a complete WAIS collapse under strong forcing, hereby contradicting Barletta et al. (2018). Another limitation of this study arises from the fact that we do not account for present-day bedrock deformation due to past ice-sheet changes when we initialize our model (i.e., the solid Earth is assumed to be in equilibrium with the initial ice load). Indeed, ongoing deformation may influence the dynamics of the future ice sheet at least until the GIA signal associated with past ice mass changes is swamped by the signal due to current and future ice losses. The response of the solid Earth to past ice and ocean mass changes tends to reduce grounding-line retreat through uplift of the bedrock (observed in WAIS and at the margins of EAIS, see Figure 4; Adhikari et al., 2014; Larour et al., 2019), meaning that mass loss might be overestimated. However, in accordance with Adhikari et al. (2014), we find that past loading is less important than future loading for the evolution of the future bed topography, with uplift rates at 2100 CE under the four RCP scenarios predicted to be significantly greater than observed present-day rates (see Supporting Information Figure S19). Nonetheless, testing the influence of our equilibrium assumption would constitute an important

improvement point for future work. Finally, an additional limitation of our approach is associated with the relatively coarse spatial resolution adopted (25 km), reducing our ability to properly capture small-scale bedrock features that may affect grounding-line migration rates, such as bedrock irregularities or ice shelf pinning points (Morlighem et al., 2019). Even though the effect of ice shelf pinning points at sub-grid resolution has been introduced through a parameterization (Pollard & DeConto, 2012a), we may expect discrepancies between our results and results at high spatial resolutions (<5 km), especially for important small ice streams and outlets. Nevertheless, multi-model ensemble estimates of future ice sheet response within ISMIP6 (Seroussi et al., 2020) clearly demonstrate that the overall behaviur of the f.ETISh model is in line with high-resolution models. High spatial resolution remains a limiting factor for studying ice sheet behaviur on longer than centennial timescales in a parameter space ensemble, as is presented here. Note that the results presented above (i) may depend on the initial conditions adopted in the simulations (Cornford et al., 2015; Seroussi et al., 2019) and (ii) are valid for the ice sheet parameters listed in Appendix A. Changes in the initial conditions and/or the values of those parameters may lead to different ice sheet response scenarios and feedback effects while not changing the overall results for an ensemble of simulations.

5 Conclusions

We developed an elementary GIA model using an adapted ELRA model that considers the regional heterogeneity in Antarctic Earth structure together with an approximation to local geoid changes due to mass changes. The model is used to investigate the sensitivity of the AIS to GIA feedbacks over the next five thousand years. This simplified model, even though it does not consider the full complexity of the GIA signal, represents a somewhat comprehensive model of regional relative sea-level changes and is easy to implement in a standalone ice-sheet model. This makes it very useful if one seeks to use a computationally-efficient model that captures the essential features and processes influencing Antarctic grounding-line stability, including the strong variability in Antarctic viscoelastic properties. It also allows for the realisation of large ensembles of simulations and parameter exploration, which is not envisageable with SVGEMs considering a 3-D Earth rheology. In this framework, we explore for the first time the complete uncertainty range in Antarctic solid-Earth characteristics in a probabilistic assessment using 2000 Monte Carlo samples spanning plausible Antarctic solid-Earth structures to assess their impact on the response of the AIS to future warming. We show that on multicentennial-to-millennial timescales, model projections that do not consider the dichotomy between West and East Antarctic solid-Earth structures overestimate (by up to 50% compared to the median response) the sea-level contribution from the AIS because regional solid-Earth deformation plays a significant role in promoting the stability of the WAIS. However, GIA feedbacks cannot prevent WAIS collapse under high-emissions climate scenarios. At longer timescales and under unabated climate forcing, future mass loss may be underestimated (by up to 40% depending on the adopted viscoelastic properties) because in East Antarctica, GIA feedbacks associated with stronger Earth models provide a reduced stabilizing effect compared with the spatially-uniform Earth deformation models typically considered in numerical ice sheet models. The pathway followed by the future AIS is very sensitive to the solid-Earth structure adopted when evaluating the solid-Earth component of GIA across Antarctica. The highest uncertainty arises from the EAIS where grounding-line retreat in the Aurora Basin is very GIA-dependent. In this context, the AIS response might be an even larger source of uncertainty in projecting sea-level rise than previously thought. If we want to robustly predict the future behavior of the AIS under warming climate, its solid-Earth structure should therefore be better constrained.

Table A1. Model symbols, units and nominal values.

Symbol	Description	Units	Value
g	Gravitational acceleration	$\mathrm{m\,s^{-2}}$	9.81
ρ_a	Asthenospheric density	$\mathrm{kg\,m^{-3}}$	3370
ρ_i	Ice density	$\mathrm{kg\,m^{-3}}$	910
ν	Poisson's ratio	-	0.25
E	Young's modulus	GPa	100
R_e	Earth's radius	m	6.378×10^6
M_e	Earth's mass	kg	5.972×10^{24}

Appendix A Model Setup

We performed simulations of the response of the AIS to environmental and parametric perturbations with the fast Elementary Thermomechanical Ice Sheet (f.ETISh) model (Pattyn, 2017) version 1.6. The f.ETISh model is a vertically-integrated, thermomechanical, hybrid ice-sheet/ice-shelf model that incorporates essential characteristics of ice-sheet thermomechanics and ice-stream flow, such as the mass-balance feedback, bedrock deformation, sub-shelf melting, and calving. The ice flow is represented as a combination of the shallow-ice (SIA) and shallow-shelf (SSA) approximations for grounded ice while only the shallow-shelf approximation is applied for floating ice shelves (Bueler & Brown, 2009; Winkelmann et al., 2011). Basal sliding is introduced as a Weertman sliding law, i.e.,

$$v_b = -A_b|\tau_b|^{m-1}\tau_b \tag{A1}$$

where τ_b is the basal shear stress, v_b the basal velocity, A_b the basal sliding coefficient – whose values are inferred following the nudging method of Pollard and DeConto (2012b) – and $m = 3$ a sliding exponent. Basal melting underneath the floating ice shelves is determined with the PICO model (Reese et al., 2018). Calving at the ice front depends on the combined penetration depths of surface and basal crevasses, relative to total ice thickness. The depths of the surface and basal crevasses are parameterized as functions of the divergence of ice velocity, the accumulated strain, the ice thickness, and surface liquid water availability, similar to Pollard et al. (2015) and DeConto and Pollard (2016). Prescribed input data include the present-day ice-sheet geometry and bedrock topography from the Bedmachine dataset (Morlighem et al., 2019) and the geothermal heat flux by Shapiro and Ritzwoller (2004). Present-day mean surface air temperature and precipitation are obtained from van Wessem et al. (2014), based on the regional atmospheric climate model RACMO2. Following Golledge et al. (2015), we assume that a 1°C increase in air temperature accounts for a 5.3% increase in precipitation. Surface temperatures are corrected for elevation changes according to a vertical lapse rate (Pollard & DeConto, 2012a). Surface melt is determined from a Positive Degree-Day model (Huybrechts & De Wolde, 1999). We employed data by Schmidtko et al. (2014) for present-day ocean temperature and salinity on the continental shelf.

Acknowledgments

We thank Wouter van der Wal and the anonymous reviewers for their thoughtful reviews. We also thank Dick Peltier for making the ICE6G_C (VM5a) model outputs available. This work was funded by the Fonds de la Recherche Scientifique de Belgique (F.R.S.-FNRS) with an F.R.S.-FNRS Research Fellowship (Violaine Coulon). Kevin Bulthuis's research was supported by an appointment to the NASA Postdoctoral Program at the

NASA Jet Propulsion Laboratory, administered by Universities Space Research Association under contract with NASA. Pippa L. Whitehouse's contribution was supported by a UK Natural Environment Research Council (NERC) Independent Research Fellowship (NE/K009958/1). This publication was supported by PROTECT. This project has received funding from the European Union's Horizon 2020 research and innovation programme under grant agreement No 869304, PROTECT contribution number 17. Computational resources have been provided by the Shared ICT Services Centre, Université Libre de Bruxelles. The data reported in this paper have been deposited in the Pangaea database. Time series from the performed Antarctic ice sheet simulations can be downloaded from https://doi.pangaea.de/10.1594/PANGAEA.911805. ELRA-modelled uplift rates with spatially-uniform and spatially-varying ELRA parameters can be downloaded from https://doi.pangaea.de/10.1594/PANGAEA.911817. The code for the Elementary GIA model is available on request from the corresponding author.

Author contributions

VC, KB and FP conceived the experiments with inputs from PLW. KB developed the ELRA model with a spatially-varying flexural rigidity. VC and FP led the paper writing, with contributions from all authors.

References

Adhikari, S., Ivins, E. R., Larour, E., Caron, L., & Seroussi, H. (2020). A kinematic formalism for tracking ice–ocean mass exchange on the earth's surface and estimating sea-level change. *The Cryosphere*, *14*(9), 2819–2833. doi: https://doi.org/10.5194/tc-14-2819-2020

Adhikari, S., Ivins, E. R., Larour, E., Seroussi, H., Morlighem, M., & Nowicki, S. (2014). Future Antarctic bed topography and its implications for ice sheet dynamics. *Solid Earth*, *5*, 569–584. doi: https://doi.org/10.5194/se-5-569-2014

Aitken, A., Roberts, J., van Ommen, T., Young, D., Golledge, N., Greenbaum, J., ... Siegert, M. (2016). Repeated large-scale retreat and advance of totten glacier indicated by inland bed erosion. *Nature*, *533*, 385-389. doi: https://doi.org/10.1038/nature17447

An, M., Wiens, D. A., Zhao, Y., Feng, M., Nyblade, A. A., Kanao, M., ... Lévêque, J. J. (2015). S-velocity model and inferred Moho topography beneath the Antarctic Plate from Rayleigh waves. *Journal of Geophysical Research: Solid Earth*, *120*(1), 359–383. doi: https://doi.org/10.1002/2014JB011332

Argus, D. F., Peltier, W. R., Drummond, R., & Moore, A. W. (2014). The Antarctica component of postglacial rebound model ICE-6G_C (VM5a) based on GPS positioning, exposure age dating of ice thicknesses, and relative sea level histories. *Geophysical Journal International*, *198*, 537–563. doi: https://doi.org/10.1093/gji/ggu140

Audet, P., & Mareschal, J.-C. (2004). Variations in elastic thickness in the Canadian Shield. *Earth and Planetary Science Letters*, *226*(1-2), 17-31. doi: https://doi.org/10.1016/j.epsl.2004.07.035

Barletta, V. R., Bevis, M., Smith, B. E., Wilson, T., Brown, A., Bordoni, A., ... Wiens, D. A. (2018). Observed rapid bedrock uplift in amundsen sea embayment promotes ice-sheet stability. *Science*, *360*(6395), 1335–1339. doi: https://doi.org/110.1126/science.aao1447

Bintanja, R., & van de Wal, R. S. (2008). North American ice-sheet dynamics and the onset of 100,000-year glacial cycles. *Nature*, *454*(August), 869–872. doi: https://doi.org/10.1038/nature07158

Brotchie, J. F., & Silvester, R. (1969). On Crustal Flexure. *Journal of Geophysical Research*, *74*(22), 5240–5252. doi: https://doi.org/10.1029/JB074i022p05240

Bueler, E., & Brown, J. (2009). Shallow shelf approximation as a "sliding law" in a thermomechanically coupled ice sheet model. *Journal of Geophysical Research: Earth Surface*, *114*(F3). doi: https://doi.org/10.1029/2008JF001179

Bueler, E., Lingle, C. S., & Brown, J. (2007). Fast computation of a viscoelastic deformable Earth model for ice-sheet simulations. *Annals of Glaciology*, *46*, 97–105. doi: https://doi.org/10.3189/172756407782871567

Bulthuis, K., Arnst, M., Sun, S., & Pattyn, F. (2019). Uncertainty quantification of the multi-centennial response of the antarctic ice sheet to climate change. *The Cryosphere*, *13*(4), 1349–1380. doi: https://doi.org/10.5194/tc-13-1349-2019

Caron, L., Ivins, E. R., Larour, E., Adhikari, S., Nilsson, J., & Blewitt, G. (2018). Gia model statistics for grace hydrology, cryosphere, and ocean science. *Geophysical Research Letters*, *45*(5), 2203-2212. doi: https://doi.org/10.1002/2017GL076644

Chen, B., Haeger, C., Kaban, M. K., & Petrunin, A. G. (2018). Variations of the effective elastic thickness reveal tectonic fragmentation of the antarctic lithosphere. *Tectonophysics*, *746*, 412 - 424. (Understanding geological processes through modelling - A Memorial Volume honouring Evgenii Burov) doi: https://doi.org/10.1016/j.tecto.2017.06.012

Clark, J. A., & Lingle, C. S. (1977). Future sea-level changes due to West Antarctic ice sheet fluctuations. *Nature*, *269*, 206–209. doi: https://doi.org/10.1038/269206a0

Cornford, S. L., Martin, D. F., Payne, A. J., Ng, E. G., Le Brocq, A. M., Gladstone, R. M., ... Vaughan, D. G. (2015). Century-scale simulations of the response of the west antarctic ice sheet to a warming climate. *The Cryosphere*, *9*(4), 1579–1600. doi: https://doi.org/10.5194/tc-9-1579-2015

de Boer, B., Dolan, A. M., Bernales, J., Gasson, E., Goelzer, H., Golledge, N. R., ... van de Wal, R. S. W. (2015). Simulating the antarctic ice sheet in the late-pliocene warm period: Plismip-ant, an ice-sheet model intercomparison project. *The Cryosphere*, *9*(3), 881–903. doi: https://doi.org/10.5194/tc-9-881-2015

de Boer, B., Stocchi, P., & van de Wal, R. S. W. (2014). A fully coupled 3-d ice-sheet–sea-level model: algorithm and applications. *Geoscientific Model Development*, *7*(5), 2141–2156. doi: https://doi.org/10.5194/gmd-7-2141-2014

de Boer, B., Stocchi, P., Whitehouse, P. L., & van de Wal, R. S. (2017). Current state and future perspectives on coupled ice-sheet – sea-level modelling. *Quaternary Science Reviews*, *169*, 13–28. doi: https://doi.org/10.1016/j.quascirev.2017.05.013

DeConto, R. M., & Pollard, D. (2016). Contribution of Antarctica to past and future sea-level rise. *Nature*, *531*, 591–597. doi: https://doi.org/10.1038/nature17145

Edwards, T. L., Brandon, M. A., Durand, G., Edwards, N. R., Golledge, N. R., Holden, P. B., ... Wernecke, A. (2019). Revisiting Antarctic ice loss due to marine ice-cliff instability. *Nature*, *566*, 58–64. doi: https://doi.org/10.1038/s41586-019-0901-4

Farrell, W. E., & Clark, J. A. (1976). On Postglacial Sea Level. *Geophysical Journal of the Royal Astronomical Society*, *46*(3), 647–667. doi: https://doi.org/10.1111/j.1365-246X.1976.tb01252.x

Favier, L., Durand, G., Cornford, S. L., Gudmundsson, G. H., Gagliardini, O., Gillet-Chaulet, F., ... Le Brocq, A. M. (2014). Retreat of Pine Island Glacier controlled by marine ice-sheet instability. *Nature Climate Change*, *4*, 117–121. doi: https://doi.org/10.1038/nclimate2094

Fjeldskaar, W. (1997). Flexural rigidity of fennoscandia inferred from the postglacial uplift. *Tectonics*, *16*(4), 596-608. doi: https://doi.org/10.1029/97TC00813

Fretwell, P., Pritchard, H. D., Vaughan, D. G., Bamber, J. L., Barrand, N. E., Bell, R., ... Zirizzotti, A. (2013). Bedmap2: Improved ice bed, surface

and thickness datasets for Antarctica. *The Cryosphere*, *7*, 375–393. doi: https://doi.org/10.5194/tc-7-375-2013

Garbe, J., Albrecht, T., Levermann, A., Donges, J., & Winkelmann, R. (2020). The hysteresis of the antarctic ice sheet. *Nature*, *585*, 538-544. doi: https://doi.org/10.1038/s41586-020-2727-5

Garcia, E. S., Sandwell, D. T., & Luttrell, K. M. (2014). An iterative spectral solution method for thin elastic plate flexure with variable rigidity. *Geophysical Journal International*, *200*(2), 1012-1028. doi: https://doi.org/10.1093/gji/ggu449

Goelzer, H., Coulon, V., Pattyn, F., de Boer, B., & van de Wal, R. (2020). Brief communication: On calculating the sea-level contribution in marine ice-sheet models. *The Cryosphere*, *14*(3), 833–840. doi: 10.5194/tc-14-833-2020

Golledge, N. R., Kowalewski, D. E., Naish, T. R., Levy, R. H., Fogwill, C. J., & Gasson, E. G. W. (2015). The multi-millennial Antarctic commitment to future sea-level rise. *Nature*, *526*(7573), 421–425. doi: https://doi.org/10.1038/nature15706

Gomez, N., Latychev, K., & Pollard, D. (2018). A Coupled Ice Sheet–Sea Level Model Incorporating 3D Earth Structure: Variations in Antarctica during the Last Deglacial Retreat. *Journal of Climate*, *31*(10), 4041-4054. doi: https://doi.org/10.1175/JCLI-D-17-0352.1

Gomez, N., Pollard, D., & Holland, D. (2015). Sea-level feedback lowers projections of future antarctic ice-sheet mass loss. *Nature Communications*, *6*, 1–8. doi: https://doi.org/10.1038/ncomms9798

Gomez, N., Pollard, D., & Mitrovica, J. X. (2013). A 3-D coupled ice sheet – sea level model applied to Antarctica through the last 40 ky. *Earth and Planetary Science Letters*, *384*, 88–99. doi: https://doi.org/10.1016/j.epsl.2013.09.042

Gomez, N., Pollard, D., Mitrovica, J. X., Huybers, P., & Clark, P. U. (2012). Evolution of a coupled marine ice sheet–sea level model. *Journal of Geophysical Research: Earth Surface*, *117*(F1). doi: https://doi.org/10.1029/2011JF002128

Gomez, N., Weber, M., Clark, P., Mitrovica, J., & Han, H. (2020). Antarctic ice dynamics amplified by northern hemisphere sea-level forcing. *Nature*, *587*, 600-604. doi: https://doi.org/10.1038/s41586-020-2916-2

Greve, R., & Blatter, H. (2009). Dynamics of ice sheets and glaciers. Berlin, Heidelberg: Springer. doi: https://doi.org/10.1007/978-3-642-03415-2

Haseloff, M., & Sergienko, O. V. (2018). The effect of buttressing on grounding line dynamics. *Journal of Glaciology*, *64*(245), 417–431. doi: https://doi.org/10.1017/jog.2018.30

Hay, C. C., Lau, H. C., Gomez, N., Austermann, J., Powell, E., Mitrovica, J. X., ... Wiens, D. A. (2017). Sea level fingerprints in a region of complex earth structure: The case of WAIS. *Journal of Climate*, *30*(6), 1881–1892. doi: https://doi.org/10.1175/JCLI-D-16-0388.1

Heeszel, D. S., Wiens, D. A., Anandakrishnan, S., Aster, R. C., Dalziel, I. W., Huerta, A. D., ... Winberry, J. P. (2016). Upper mantle structure of central and West Antarctica from array analysis of Rayleigh wave phase velocities. *Journal of Geophysical Research: Solid Earth*, *121*(3), 1758–1775. doi: https://doi.org/10.1002/2015JB012616

Huybrechts, P., & De Wolde, J. (1999). The dynamic response of the Greenland and Antarctic ice sheets to multiple-century climatic warming. *Journal of Climate*, *12*(8), 2169–2188. doi: https://doi.org/10.1175/1520-0442(1999)012⟨2169:TDROTG⟩2.0.CO;2

Joughin, I., Smith, B. E., & Medley, B. (2014). Marine ice sheet collapse potentially under way for the thwaites glacier basin, west antarctica. *Science*, *344*(6185), 735–738. doi: https://doi.org/10.1126/science.1249055

Kachuck, S. B., Martin, D. F., Bassis, J. N., & Price, S. F. (2020). Rapid viscoelastic deformation slows marine ice sheet instability at pine island

glacier. *Geophysical Research Letters*, *47*(10), e2019GL086446. doi: https://doi.org/10.1029/2019GL086446

Kaufmann, G., Wu, P., & Ivins, E. R. (2005). Lateral viscosity variations beneath Antarctica and their implications on regional rebound motions and seismotectonics. *Journal of Geodynamics*, *39*(2), 165–181. doi: https://doi.org/10.1016/j.jog.2004.08.009

Kingslake, J., Scherer, R., Albrecht, T., Coenen, J., Powell, R., Reese, R., ... Whitehouse, P. (2018). Extensive retreat and re-advance of the west antarctic ice sheet during the holocene. *Nature.*, *558*(7710), 430–434. doi: https://doi.org/10.1038/s41586-018-0208-x

Konrad, H., Sasgen, I., Klemann, V., Thoma, M., Grosfeld, K., & Martinec, Z. (2016). Sensitivity of grounding-line dynamics to viscoelastic deformation of the solid-earth in an idealized scenario. *Polarforschung*, *85*(2), 89–99. doi: https://doi.org/10.2312/polfor.2016.005

Konrad, H., Sasgen, I., Pollard, D., & Klemann, V. (2015). Potential of the solid-Earth response for limiting long-term West Antarctic Ice Sheet retreat in a warming climate. *Earth and Planetary Science Letters*, *432*, 254–264. doi: https://doi.org/10.1016/j.epsl.2015.10.008

Konrad, H., Thoma, M., Sasgen, I., Klemann, V., Grosfeld, K., Barbi, D., & Martinec, Z. (2014). The Deformational Response of a Viscoelastic Solid Earth Model Coupled to a Thermomechanical Ice Sheet Model. *Surveys in Geophysics*, *35*(6), 1441–1458. doi: https://doi.org/10.2312/polfor.2016.005

Lambeck, K., Rouby, H., Purcell, A., Sun, Y., & Sambridge, M. (2014). Sea level and global ice volumes from the Last Glacial Maximum to the Holocene. *PNAS*, *111*(43), 15296–15303. doi: https://doi.org/10.1073/pnas.1411762111

Larour, E., Seroussi, H., Adhikari, S., Ivins, E., Caron, L., Morlighem, M., & Schlegel, N. (2019). Slowdown in antarctic mass loss from solid earth and sea-level feedbacks. *Science*, *364*(6444). doi: https://doi.org/10.1126/science.aav7908

Le Meur, E., & Huybrechts, P. (1996). A comparison of different ways of dealing with isostasy: examples from modelling the Antarctic ice sheet during the last glacial cycle. *Annals of Glaciology*, *23*, 309–317. doi: https://doi.org/10013/epic.12717.d001

Lingle, C. S., & Clark, J. A. (1985). A numerical model of interactions between a marine ice sheet and the solid earth: Application to a West Antarctic ice stream. *Journal of Geophysical Research*, *90*(C1), 1100. doi: https://doi.org/10.1029/JC090iC01p01100

Lloyd, A. J., Wiens, D. A., Zhu, H., Tromp, J., Nyblade, A. A., Aster, R. C., ... O'Donnell, J. P. (2020). Seismic structure of the antarctic upper mantle imaged with adjoint tomography. *Journal of Geophysical Research: Solid Earth*, *125*(3). doi: https://doi.org/10.1029/2019JB017823

Lowrie, W. (2007). *Fundamentals of geophysics* (2nd ed.). Cambridge University Press. doi: https://doi.org/10.1017/CBO9780511807107

Maris, M. N. A., de Boer, B., Ligtenberg, S. R. M., Crucifix, M., van de Berg, W. J., & Oerlemans, J. (2014). Modelling the evolution of the Antarctic ice sheet since the last interglacial. *The Cryosphere*, *8*, 1347–1360. doi: https://doi.org/10.5194/tc-8-1347-2014

Matsuoka, K., Hindmarsh, R. C., Moholdt, G., Bentley, M. J., Pritchard, H. D., Brown, J., ... Whitehouse, P. L. (2015). Antarctic ice rises and rumples: Their properties and significance for ice-sheet dynamics and evolution. *Earth-Science Reviews*, *150*, 724-745. doi: https://doi.org/10.1016/j.earscirev.2015.09.004

Mercer, J. H. (1978). West Antarctic ice sheet and CO2 greenhouse effect: a threat of disaster. *Nature*, *271*, 321–325. doi: https://doi.org/10.1038/271321a0

Milne, A., Glenn, & Mitrovica, X., Jerry. (1998). Postglacial sea-level change on a

rotating earth. *Geophysical Journal International*, *133*(1), 1-19. doi: https://doi.org/10.1046/j.1365-246X.1998.1331455.x

Mitrovica, J. X., Tamisiea, M. E., Davis, J. L., & Milne, G. A. (2001). Recent mass balance of polar ice sheets inferred from patterns of global sea-level change. *Nature*, *409*, 1026–1029. doi: https://doi.org/10.1038/35059054

Morelli, A., & Danesi, S. (2004). Seismological imaging of the Antarctic continental lithosphere: A review. *Global and Planetary Change*, *42*(1-4), 155–165. doi: https://doi.org/10.1016/j.gloplacha.2003.12.005

Morlighem, M., Rignot, E., Binder, T., Blankenship, D., Drews, R., Eagles, G., ... Smith, E. C. (2019). Deep glacial troughs and stabilizing ridges unveiled beneath the margins of the Antarctic ice sheet. *Nature Geoscience*. doi: https://doi.org/10.1038/s41561-019-0510-8

Nield, G. A., Barletta, V. R., Bordoni, A., King, M. A., Whitehouse, P. L., Clarke, P. J., ... Berthier, E. (2014). Rapid bedrock uplift in the Antarctic Peninsula explained by viscoelastic response to recent ice unloading. *Earth and Planetary Science Letters*, *397*, 32–41. doi: https://doi.org/10.1016/j.epsl.2014.04.019

Nield, G. A., Whitehouse, P. L., Wal, W. V. D., Blank, B., Donnell, P. O., & Stuart, G. W. (2018). The impact of lateral variations in lithospheric thickness on glacial isostatic adjustment in West Antarctica. *Geophysical Journal International*, *214*, 811–824. doi: https://doi.org/10.1093/gji/ggy158

Pappa, F., Ebbing, J., Ferraccioli, F., & van der Wal, W. (2019). Modeling satellite gravity gradient data to derive density, temperature, and viscosity structure of the antarctic lithosphere. *Journal of Geophysical Research: Solid Earth*, *124*(11), 12053-12076. doi: https://doi.org/10.1029/2019JB017997

Pattyn, F. (2017). Sea-level response to melting of Antarctic ice shelves on multi-centennial timescales with the fast Elementary Thermomechanical Ice Sheet model (f.ETISh v1.0). *Cryosphere*, *11*, 1–28. doi: https://doi.org/10.5194/tc-11-1-2017

Pattyn, F., Perichon, L., Durand, G., Favier, L., Gagliardini, O., Hindmarsh, R. C. a., ... Wilkens, N. (2013). Grounding-line migration in plan-view marine ice-sheet models: Results of the ice2sea MISMIP3d intercomparison. *Journal of Glaciology*, *59*, 410–422. doi: https://doi.org/10.3189/2013JoG12J129

Pegler, S. S. (2018). Suppression of marine ice sheet instability. *Journal of Fluid Mechanics*, *857*, 648–680. doi: https://doi.org/10.1017/jfm.2018.742

Perez-Gussinye, M., & Watts, A. (2005). The long-term strength of europe and its implications for plate-forming processes. *Nature*, *436*, 381-4. doi: https://doi.org/10.1038/nature03854

Pollard, D., & DeConto, R. M. (2012a). Description of a hybrid ice sheet-shelf model , and application to Antarctica. *Geoscientific Model Development*, *5*, 1273–1295. doi: https://doi.org/10.5194/gmd-5-1273-2012

Pollard, D., & DeConto, R. M. (2012b). A simple inverse method for the distribution of basal sliding coefficients under ice sheets , applied to Antarctica. *The Cryosphere*, *6*, 953–971. doi: https://doi.org/10.5194/tc-6-953-2012

Pollard, D., & DeConto, R. M. (2020). Improvements in one-dimensional grounding-line parameterizations in an ice-sheet model with lateral variations (psuice3d v2.1). *Geoscientific Model Development*, *13*(12), 6481–6500. doi: https://doi.org/10.5194/gmd-13-6481-2020

Pollard, D., DeConto, R. M., & Alley, R. B. (2015). Potential Antarctic Ice Sheet retreat driven by hydrofracturing and ice cliff failure. *Earth and Planetary Science Letters*, *412*, 112–121. doi: https://doi.org/10.1016/j.epsl.2014.12.035

Pollard, D., Gomez, N., & Deconto, R. M. (2017). Variations of the antarctic ice sheet in a coupled ice sheet-earth-sea level model: Sensitivity to viscoelastic earth properties. *Journal of Geophysical Research: Earth Surface*, *122*(11), 2124-2138. doi: https://doi.org/10.1002/2017JF004371

Powell, E., Gomez, N., Hay, C., Latychev, K., & Mitrovica, J. X. (2020). Viscous

Effects in the Solid Earth Response to Modern Antarctic Ice Mass Flux : Implications for Geodetic Studies of WAIS Stability in a Warming World. *Journal of Climate*, *33*, 443–459. doi: https://doi.org/10.1175/JCLI-D-19-0479.1

Pueyo, S. (2012). Solution to the paradox of climate sensitivity. *Climatic Change*, *113*(April 2011), 163–179. doi: https://doi.org/10.1007/s10584-011-0328-x

Quiquet, A., Dumas, C., Ritz, C., Peyaud, V., & Roche, D. M. (2018). The GRISLI ice sheet model (version 2.0): calibration and validation for multi-millennial changes of the antarctic ice sheet. *Geoscientific Model Development*, *11*(12), 5003–5025. doi: https://doi.org/10.5194/gmd-11-5003-2018

Reese, R., Albrecht, T., Mengel, M., Asay-Davis, X., & Winkelmann, R. (2018). Antarctic sub-shelf melt rates via pico. *The Cryosphere*, *12*(6), 1969–1985. Retrieved from `https://tc.copernicus.org/articles/12/1969/2018/` doi: https://doi.org/10.5194/tc-12-1969-2018

Rignot, E., Mouginot, J., Scheuchl, B., van den Broeke, M., van Wessem, M. J., & Morlighem, M. (2019). Four decades of antarctic ice sheet mass balance from 1979–2017. *Proceedings of the National Academy of Sciences*, *116*(4), 1095–1103. doi: https://doi.org/10.1073/pnas.1812883116

Ritz, C., Edwards, T. L., Durand, G., Payne, A. J., Peyaud, V., & Hindmarsh, R. C. A. (2015). Potential sea-level rise from Antarctic ice-sheet instability constrained by observations. *Nature*, *528*(7580), 115–118. doi: https://doi.org/10.1038/nature16147

Ritzwoller, M. H., Shapiro, N. M., Levshin, A. L., & Leahy, G. M. (2001). Crustal and upper mantle structure beneath antarctica and surrounding oceans. *Journal of Geophysical Research: Solid Earth*, *106*(B12), 30645-30670. doi: https://doi.org/10.1029/2001JB000179

Robert & Casella, G. (2013). *Monte Carlo statistical methods* (2nd ed.). New York, NY:: Springer Science & Business Media. doi: https://doi.org/10.1007/978-1-4757-4145520-2

Root, B. C., van der Wal, W., Novák, P., Ebbing, J., & Vermeersen, L. L. A. (2015). Glacial isostatic adjustment in the static gravity field of fennoscandia. *Journal of Geophysical Research: Solid Earth*, *120*(1), 503-518. doi: https://doi.org/10.1002/2014JB011508

Saltelli, A., Ratto, M., Andres, T., Campolongo, F., Cariboni, J., Gatelli, D., & Tarantola, S. (2008). *Global Sensitivity Analysis: The Primer*. West Sussex, United Kingdom: John Wiley & Sons. doi: https://doi.org/10.1002/9780470725184

Scambos, T., Bell, R., Alley, R., Anandakrishnan, S., Bromwich, D., Brunt, K., ... Yager, P. (2017). How much, how fast?: A science review and outlook for research on the instability of antarctica's thwaites glacier in the 21st century. *Global and Planetary Change*, *153*, 16 - 34. doi: https://doi.org/10.1016/j.gloplacha.2017.04.008

Schmidtko, S., Heywood, K. J., Thompson, A. F., & Aoki, S. (2014). Multidecadal warming of Antarctic waters. *Science*, *346*(6214), 1227–1231. doi: https://doi.org/10.1126/science.1256117

Schoof, C. (2007). Ice sheet grounding line dynamics: Steady states, stability, and hysteresis. *Journal of Geophysical Research: Earth Surface*, *112*, 1–19. doi: https://doi.org/10.1029/2006JF000664

Scott, D. W. (2015). *Multivariate density estimation: Theory, practice, and visualization,*. Rice University, Houston, Texas: John Wiley & Sons, Inc. doi: https://doi.org/10.1002/9781118575574

Sergienko, O. V., & Wingham, D. J. (2019). Grounding line stability in a regime of low driving and basal stresses. *Journal of Glaciology*, *65*(253), 833–849. doi: https://doi.org/10.1017/jog.2019.53

Seroussi, H., Nowicki, S., Payne, A. J., Goelzer, H., Lipscomb, W. H., Abe-Ouchi, A., ... Zwinger, T. (2020). Ismip6 antarctica: a multi-model ensemble of the

antarctic ice sheet evolution over the 21st century. *The Cryosphere*, *14*(9), 3033–3070. doi: https://doi.org/10.5194/tc-14-3033-2020

Seroussi, H., Nowicki, S., Simon, E., Abe-Ouchi, A., Albrecht, T., Brondex, J., ... Zhang, T. (2019). initmip-antarctica: an ice sheet model initialization experiment of ismip6. *The Cryosphere*, *13*(5), 1441–1471. doi: https://doi.org/10.5194/tc-13-1441-2019

Shapiro, N. M., & Ritzwoller, M. H. (2004). Inferring surface heat flux distributions guided by a global seismic model : particular application to Antarctica. *Earth and Planetary Science Letters*, *223*, 213–224. doi: https://doi.org/10.1016/j.epsl.2004.04.011

Stern, T. A., & ten Brink, U. S. (1989). Flexural uplift of the Transantarctic Mountains. *Journal of Geophysical Research: Solid Earth*, *94*(B8), 10315–10330. doi: https://doi.org/10.1029/JB094iB08p10315

Sun, S., Pattyn, F., Simon, E. G., Albrecht, T., Cornford, S., Calov, R., ... et al. (2020). Antarctic ice sheet response to sudden and sustained ice-shelf collapse (abumip). *Journal of Glaciology*, *66*(260), 891–904. doi: https://doi.org/10.1017/jog.2020.67

Thomas, R. H., & Bentley, C. R. (1978). A Model for Holocene Retreat of the West Antarctic Ice Sheet. *Quaternary Research*, *10*(2), 150–170. doi: https://doi.org/10.1016/0033-5894(78)90098-4

Turcotte, D. L., & Schubert, G. (2002). *Geodynamics* (2nd ed.). Cambridge: Cambridge University Press. doi: https://doi.org/10.1017/CBO9780511807442

van der Wal, W., Whitehouse, P. L., & Schrama, E. J. (2015). Effect of GIA models with 3D composite mantle viscosity on GRACE mass balance estimates for Antarctica. *Earth and Planetary Science Letters*, *414*, 134–143. doi: https://doi.org/10.1016/j.epsl.2015.01.001

Van Wees, J. D., & Cloetingh, S. (1994). A finite-difference technique to incorporate spatial variations in rigidity and planar faults into 3-d models for lithospheric flexure. *Geophysical Journal International*, *117*(1), 179-195. doi: https://doi.org/10.1111/j.1365-246X.1994.tb03311.x

van Wessem, J. M. V., Reijmer, C. H., Lenaerts, J. T. M., Berg, W. J. V. D., van den Broeke, M. R. V. D., & van Meijgaard, E. (2014). Updated cloud physics in a regional atmospheric climate model improves the modelled surface energy balance of Antarctica. *The Cryosphere*, *8*, 125–135. doi: https://doi.org/10.5194/tc-8-125-2014

Ventsel, E., & Krauthammer, T. (2001). *Thin plates and shells* (1st ed.). Boca Raton: CRC Press. doi: https://doi.org/10.1201/9780203908723

Walcott, R. I. (1970). Flexural rigidity, thickness, and viscosity of the lithosphere. *Journal of Geophysical Research (1896-1977)*, *75*(20), 3941-3954. doi: https://doi.org/10.1029/JB075i020p03941

Weertman, J. (1974). Stability of the junction of an ice sheet and an ice shelf. *Journal of Glaciology*, *13*, 3–11. doi: https://doi.org/10.3189/S0022143000023327

Whitehouse, P. L., Bentley, M. J., & Le Brocq, A. M. (2012). A deglacial model for antarctica: geological constraints and glaciological modelling as a basis for a new model of antarctic glacial isostatic adjustment. *Quaternary Science Reviews*, *32*, 1 - 24. doi: https://doi.org/10.1016/j.quascirev.2011.11.016

Whitehouse, P. L., Bentley, M. J., Milne, G. A., King, M. A., & Thomas, I. D. (2012). A new glacial isostatic adjustment model for antarctica: calibrated and tested using observations of relative sea-level change and present-day uplift rates. *Geophysical Journal International*, *190*(3), 1464-1482. doi: https://doi.org/10.1111/j.1365-246X.2012.05557.x

Whitehouse, P. L., Wiens, D. A., Gomez, N., & King, M. A. (2019). Solid Earth change and the evolution of the Antarctic Ice Sheet. *Nature Communications*, 1–14. doi: https://doi.org/10.1038/s41467-018-08068-y

Winkelmann, R., Martin, M. A., Haseloff, M., Albrecht, T., Bueler, E., Khroulev,

C., & Levermann, A. (2011). The potsdam parallel ice sheet model (pismpik) – part 1: Model description. *The Cryosphere*, *5*(3), 715–726. doi: https://doi.org/10.5194/tc-5-715-2011

Wolf, D. (1984). The relaxation of spherical and flat maxwell earth models and effects due to presence of the lithosphere. *J. Geophys.*, *56*, 24-33.

Wu, P., & Johnston, P. (1998). Validity of using flat-earth finite element models in the study of postglacial rebound. In *Dynamics of the ice age earth: A modern perspective* (pp. 191–202). Trans Tech Publications Limited.

Wu, P., & Peltier, W. R. (1982). Viscous gravitational relaxation. *Geophysical Journal of the Royal Astronomical Society*, *70*(2), 435-485. doi: https://doi.org/10.1111/j.1365-246X.1982.tb04976.x

References From the Supporting Information

Hertz, H. (1884). Ueber das gleichgewicht schwimmender elastischer platten. *Annalen der Physik*, 258 (7), 449-455. doi: https://doi.org/10.1002/andp.18842580711

Nadai, A. (1963). Theory of flow and fracture of solids. In (Vol. 2). New York, NY:McGraw-Hill Book Company.